

RF Coupling Revisited

Grant No. N00014 -17-1-2932

Final Report

Period of Performance: September 1, 2017 to August 31, 2021

Prepared by:

Associate Professor: Ahmed M Hassan, Co-Principal Investigator
University of Missouri, Kansas City, MO
Computer Science Electrical Engineering
5110 Rockhill Rd.
Flarsheim Hall, Room 560G-1
Kansas City, MO 64110
Tel: (816) 235-6219
Fax: (816) 235-5159
Email: hassanam@umkc.edu

Reviewed by:

Professor Anthony Caruso, Principal Investigator
University of Missouri, Kansas City, MO
Department of Physics and Astronomy
5110 Rockhill Rd.
Flarsheim Hall, Room 257
Kansas City, MO 64110
Tel: (816) 235-2505
Fax: (816) 235-5221
Email: carusoan@umkc.edu



This work was sponsored by the Office of Naval Research (ONR), under grant number N00014 - 17-1-2932. The views and conclusions contained herein are those of the authors only and should not be interpreted as representing those of ONR, the U.S. Navy or the U.S. Government.

U // Distribution A

REPORT DOCUMENTATION PAGE			Form Approved OMB No. 0704-0188		
<p>The public reporting burden for this collection of information is estimated to average 1 hour per response, including the time for reviewing instructions, searching existing data sources, gathering and maintaining the data needed, and completing and reviewing the collection of information. Send comments regarding this burden estimate or any other aspect of this collection of information, including suggestions for reducing the burden, to Department of Defense, Washington Headquarters Services, Directorate for Information Operations and Reports (0704-0188), 1215 Jefferson Davis Highway, Suite 1204, Arlington, VA 22202-4302. Respondents should be aware that notwithstanding any other provision of law, no person shall be subject to any penalty for failing to comply with a collection of information if it does not display a currently valid OMB control number.</p> <p>PLEASE DO NOT RETURN YOUR FORM TO THE ABOVE ADDRESS.</p>					
1. REPORT DATE (DD-MM-YYYY) 27-01-2021		2. REPORT TYPE Final Report		3. DATES COVERED (From - To) SEPT2017 - AUG2021	
4. TITLE AND SUBTITLE RF Coupling Revisited			5a. CONTRACT NUMBER		
			5b. GRANT NUMBER N00014-17-2932		
			5c. PROGRAM ELEMENT NUMBER		
6. AUTHOR(S) Ahmed M. Hassan, Mohamed Z. M. Hamdalla, John Lancaster, Benjamin Bissen, Kalyan Durbhakula, Khulud Alsultan, Caylin Hartshorn, Thomas Ory, Waleed Al-Shaikhli, Clayton Kettlewell, James D. Hunter, Yuanzhuo Liu, Deb Chatterjee, Praveen Rao, Victor Khilkevich, Daryl G. Beetner, Anthony N. Caruso			5d. PROJECT NUMBER		
			5e. TASK NUMBER		
			5f. WORK UNIT NUMBER		
7. PERFORMING ORGANIZATION NAME(S) AND ADDRESS(ES) University of Missouri- Kansas City 5110 Rockhill Rd Kansas City, MO 64110			8. PERFORMING ORGANIZATION REPORT NUMBER		
9. SPONSORING/MONITORING AGENCY NAME(S) AND ADDRESS(ES) Office of Naval Research One Liberty Center, 875 N Randolph Arlington, VA 22203			10. SPONSOR/MONITOR'S ACRONYM(S) ONR		
			11. SPONSOR/MONITOR'S REPORT NUMBER(S)		
12. DISTRIBUTION/AVAILABILITY STATEMENT Distribution Statement A. Approved for public release: distribution unlimited.					
13. SUPPLEMENTARY NOTES					
14. ABSTRACT The main goal of this work is to develop a joint computational/experimental approach to predict, quantify, and prove the coupling of microwaves to any arbitrary collection/geometry of wires/traces/wire-bonds in different surroundings. The computational approach is based on the Characteristic Mode Analysis (CMA) and the Equivalent Circuit Approach (ECA). The developed computational tools are combined into a single user-friendly package named "PECNEC: Predictive-package for Electromagnetic Coupling to Nonlinear-electronics using Equivalent-circuits & Characteristic-modes." The objective of PECNEC is to predict the waveform that will cause electronic upset, by maximizing the coupled voltage and power, to permutations of linear/non-linear loads in any wire topology/geometry. General guidelines obtained from the computational tools are presented, and future directions to advance PECNEC are also outlined.					
15. SUBJECT TERMS					
16. SECURITY CLASSIFICATION OF:			17. LIMITATION OF ABSTRACT SAR	18. NUMBER OF PAGES	19a. NAME OF RESPONSIBLE PERSON Anthony Caruso
a. REPORT U	b. ABSTRACT U	c. THIS PAGE U			19b. TELEPHONE NUMBER (Include area code) 816-235-2505

U // Distribution A

Distribution List ADDRESSEE	DODAAD CODE	QUANTITY
Ryan Hoffman AIR WARFARE & WEAPONS APPL DIV 875 N. Randolph Street Arlington VA 22203-1995 Phone: 703-696-3873 EMAIL: RYAN.HOFFMAN@NAVY.MIL	352	1
ONR REG Office Chicago* Telephone: (312) 886-5423 230 South Dearborn CHICAGO IL 60604-1595 *Transmittal letter only	N62880	1
DEFENSE TECHNICAL INFORMATION CENTER 8725 JOHN J. KINGMAN RD SUITE 0944 FORT BELVOIR, VA 22060-6218 E-mail: TR@dtic.mil	HJ4701	2
DIRECTOR, NAVAL RESEARCH LAB ATTN: CODE 5596 4555 OVERLOOK AVENUE, SW WASHINGTON, D.C. 20375-5320 E-mail: reports@library.nrl.navy.mil	N00173	1

Grant or Contract Number: N00014-17-1-2932

Date Prepared: 01/31/2021

Project Title: RF Coupling Re-visited

Annual Summary Report: FY2020

Principle Investigator: Anthony N. Caruso, 816-235-2505, carusoan@umkc.edu

Department of Physics and Astronomy

University of Missouri-Kansas City (UMKC), MO.

Section I: Project Summary

1. Overview of Project

Abstract:

The problem of undesirable RF coupling to wires and electronics has been receiving high interest for several decades. Coupling can be unintentional, originating from nearby radiators, especially in the rising congestion in the wireless spectrum, or due to the rising threat of High Power Microwave (HPM) weapons. In this work, we develop a combined experimental and modeling approach to quantify coupling to realistic wire systems and we also develop general guidelines to protect wires and electronic circuitry from unintentional and intentional interference.

Objective:

The objective of the proposed work is to develop rules-of-thumb to predict HPM source dependent effect coupling parameters, for any arbitrary collection/geometry of wires/traces/wire-bonds, in a dielectric or metallic enclosure. Such studies are directly applicable to unmanned aerial vehicles (UAVs) or circuits composed of PCB's/wire-bundles. The work is a combined experimental, simulation and theory effort.

The underlying physics is based on the fundamental modes or eigen-currents induced in sections of wire(s) from impinging RF, and their nearest neighbor interactions. This may be viewed as charge flowing through a scatterer, which can be decomposed into a weighted summation of fundamental modes. It is the support and strength of these modes that form the basis for their frequency-dependent coupling and primary/secondary induction.

The current-state-of-research in RF effects/coupling work focuses on the prediction of the statistical coupling properties, which can be set up within arbitrary enclosures. Such efforts do not address the actual coupling to the electronics within these enclosures, although that is the future-art in development.

Introduction:

Electromagnetic weapons in the radio frequency range (700-MHz to 95-GHz) at on-target power densities that induce tenths- to ones-of-volts onto a printed circuit board trace, free wire, or other integrated circuit input (hereafter high-power microwaves or HPM) represent a single event effect (SEE) threat to microelectronics and their downstream applications. Developing a deeper understanding of how HPM couple to wires, traces, chasses, integrated circuits, and/or their enclosures, as a function of the source properties, is the objective of this proposed effort. A stretch objective is to understand further the secondary and tertiary coupling effects, including direct and

U // Distribution A

inductive coupling. At the conclusion of this work, the vision is a balance of empirical- and simulation-derived results that will drive a generally applicable and pragmatic model (i.e., rules-of-thumb) that may be used to inform both the offensive and defensive side of HPM design and electronics and their enclosures.

Since at least the mid-1960s through today, electronic warfare – and to a lesser extent HPM – testing has been a staple for what is now MIL STD 464C. Empirical testing has been, and will likely continue to be, used as there is no current ability to generate sufficient (i.e., simple, but mostly accurate) models. This effects testing has been employed against assets ranging from motor vehicles to desktop computers to unmanned aerial vehicles to smartphones to instrument landing systems. While with enough detail and empirical feedback data, some models have been developed, but the models are not generalizable. Of those models that seek to be generalizable, they are too complicated to set up, inaccurate and/or ill-pragmatic. A new approach, which stands on the shoulders of this previous work, but harnesses the utility/power of new capabilities, is needed.

These new capabilities, whose confluence will take the above work to a new level, include the ability to: (a) map or predict the three-dimensional layout of complex electrical structures (e.g., wiring harness but not necessarily multilayer printed circuit boards); (b) automatically transfer the physical maps into simulation; (c) automatically approximate the complex permittivity/permeability of the materials; (d) run multi-source-parameter permutations on supercomputers inexpensively (through the ability to parallelize and run on an order-of-magnitude more cores/memory than two years earlier); (e) validate simulations through automated empirical measurements; and, (f) most of all, use machine learning methods to extract trends that the humans cannot.

In this work, we will design, build and test, an empirical measurement and simulation system capable of demonstrating the new capabilities described above to develop a predictive capability that is both simple and accurate enough to be useful for HPM effects and design needs.

Background:

One of the main techniques for predicting interference in metallic enclosures is the Random Coupling Model (RCM). The RCM addresses enclosures or cavities that are much larger than the wavelength of concern. Under this condition, the wave propagation inside the cavity is chaotic, meaning that any small change in the cavity or its components will lead to profoundly different outcomes. Based on the properties of the enclosure or cavity, such as its quality factor, statistical information about the voltages generated at the ports can be induced. In RCM, the ports can represent apertures in the enclosures or the input ports of devices and electronic circuitry inside the enclosure. Therefore, RCM aims to quantify the statistics of the interactions between the enclosures and its constituents. There are a number of other models (e.g., Dynamical Energy Analysis) and their predecessors that are important and form the basis for the work proposed here. We refer the reader to an exhaustive compilation of these works if greater background is desired (<http://anlge.umd.edu/RCM/>) as it is important that we shift gears to describe the background of the new effort proposed here.

The main goal of this work is to develop a joint computational/experimental approach to predict, quantify, and prove the coupling of microwaves to any arbitrary collection/geometry of

wires/traces/wire-bonds in different surroundings. The computational approach is based on the Characteristic Mode Analysis (CMA) and the Equivalent Circuit Approach (ECA).

If a scatterer is excited by an incident plane wave, currents are excited on its surface based on its conductivity. The CMA decomposes this excited current on the scatterer in terms of a set of fundamental modes [1]. These fundamental modes are independent of the excitation and they only depend on the shape, size, material, and the environment of the scatterer. Moreover, CMA provides the Modal Significance (MS_n) spectrum and the radiation characteristics of each mode. The MS_n spectrum quantifies the importance of each mode at every frequency. The radiation characteristics of each mode identify the optimum directions to excite the mode of interest. Therefore, the knowledge of the MS_n and the radiation characteristics of the modes allows the prediction of the optimum frequencies and incident directions to maximize the coupling and interference to a Devices Under Test (DUT).

The ECA approach is based on the fact that any antenna in the receiving mode, or in our case a wiring system through which back-door RF coupling can occur, can be replaced by the classical Thévenin circuit shown in Fig. 1 [2]-[5]. The Thévenin equivalent circuit involves two main components defined at the receiving port of the antenna or the wiring system: (i) the open-circuit voltage, V_{oc} , and (ii) the input impedance Z_{in} [2]. The input impedance Z_{in} is typically replaced by an equivalent circuit as shown in Fig. 2. For typical antennas, the equivalent circuit consists of a series of parallel RLC circuits. Typically, one RLC circuit is needed for each resonance in the frequency band of interest. The V_{oc} can be calculated by simulating the receiving antenna or the wiring system terminated with a very large load, ideally infinite. If a frequency-domain solver is used, the time domain V_{oc} can be easily achieved via an inverse Fourier Transform.

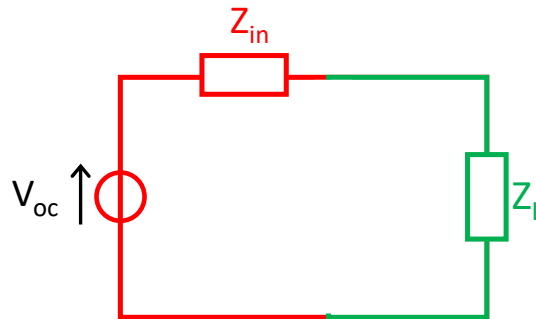


Fig. 1: Thévenin equivalent circuit of coupling to a wire system [1].

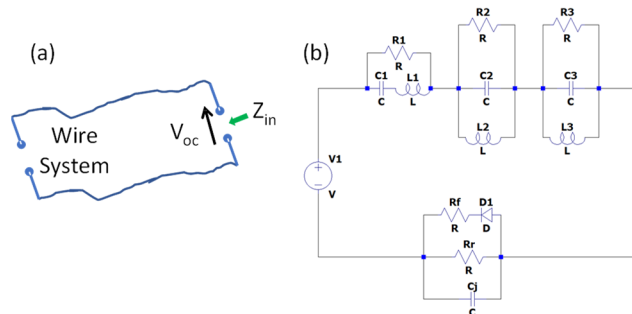


Fig. 2: (a) Dipole-like wire system and (b) the circuit that

The advantages of the equivalent circuit approach in Fig. 1 and Fig. 2 are:

1. It provides physical insight into the response of the wiring system. For example, if the equivalent circuit of a wiring system contains larger capacitance values, then it will quickly discharge the currents and voltages generated by a short pulse high power electronic microwave (HP EM) excitation preventing the buildup of energy in the nonlinear devices.

2. The above approach involves performing one full-wave simulation to calculate the V_{oc} and Z_{in} of the wiring system. After that, we can use much faster circuits simulations to simulate RF coupling to hundreds of possible nonlinear loads that can be connected to the wiring system. These simulations will be much faster when performed using a circuits solver such as LTSPICE than if they were performed using a full-wave solver. Also, this will allow us to simulate, in a feasible computational time, practical electronics and microcontrollers which tens of components.
3. The equivalent circuit approach allows the simulation of excitation of long duration that is infeasible to accomplish using full-wave solvers that enforce a small time step

In this work, we will use a novel approach that hybridizes the CMA and the ECA to predict RF coupling to wiring systems with nonlinear loads in realistic environments. All modeling and computational predictions are validated with unique experimental coupling measurements inside a Gigahertz Transverse Electromagnetic (GTEM) cell.

Activities and Accomplishments

2. Activities and Accomplishments

Coupling to an individual unterminated wire with arbitrary shape: A Characteristic Mode Analysis (CMA) Approach

Practical wiring systems typically exhibit non-straight wires or metallic traces. Therefore, the effect of wire shapes needs to be quantified to accurately assess the field-to-wire coupling and crosstalk in practical wiring systems. One of the approaches of constructing these arbitrary wires is the Random Walking Chains (RWC) model [6]. In RWC, each wire is divided into equal segments with a pre-defined length. Each segment changes its direction, by randomly varying its alignment angle β as shown in Fig. 1. By controlling the length of the segments and

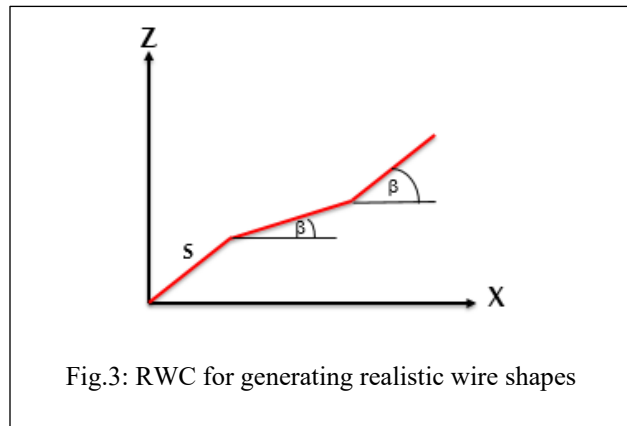


Fig.3: RWC for generating realistic wire shapes

the range of variations in the angle β , a large variety of random wire shapes with varying waviness or curvature can be generated. These angles could be solid angles, with arbitrary orientations, in order to have realistic 3-D shape variations. We started by simulating unterminated wires in free space. We chose 11 different β ranges, which correspond to 11 different levels of waviness, and for each β range, 100 different shapes were generated. For small variation in (β) the wires are very close to being straight whereas they become more crumpled as the β variations increased.

To explain the variations in the field to wire coupling, we performed the Characteristic Mode Analysis of the wires decomposing the response into the first three fundamental modes. At low frequencies, where the incident wavelength is much larger than the size of the wire, the first mode dominate the response. As the frequency of the incident wave increases, higher order modes start

U // Distribution A

to contribute to the overall response. We focused on the first 3 modes since they showed similar behavior as the wires became more-wavy due to the increase in β in the RWC model. The results showed that as the wires became more crumpled, there was a slight increase in the average resonance frequency of the wire, a significant decrease in the bandwidth of each mode, an increase in the amplitude of each modal current. Therefore, CMA explains why, on average, crumpled wires have larger coupling currents than straight wires.

To validate that unterminated nonstraight crumpled wires exhibit higher coupling on average than straight wires of the same size we simulated the two cases in Fig. 4 which shows a straight wire versus a C-shaped wire with a high curvature. Both wires in Fig. 4 have exactly the same length (1 m), radius (0.25 mm), and both are assumed to be perfectly conducting. We showed in Fig. 5 that the average coupling current to the C-shaped wire in Fig. 4b is higher than the coupling current to the straight wire in Fig. 4a since the C-shaped wire has a larger waviness level. Both wires were excited using plane waves incident at multiple directions with different electric

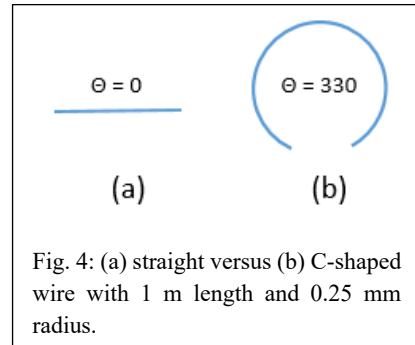


Fig. 4: (a) straight versus (b) C-shaped wire with 1 m length and 0.25 mm radius.

field polarizations. A total of 1296 angles, 36 azimuth angles and 36 elevation angles, were simulated and the average coupling current calculated. Fig. 5 shows the average coupled current to C-shaped wire versus the average coupled current to a straight wire. At the first resonance frequency, ~ 150 MHz, the average coupled current of a C-shaped wire with high curvature is 37.5% higher than that of a straight wire as shown in Fig 5. This can be explained by CMA showing that the modal currents of a wire with a higher curvature are larger in amplitude than that of a straight wire. For C-shaped wires, the resonances have a narrower bandwidth than that of a straight wire and the resonances occur at slightly higher frequencies. Again, this follows directly from the CMA which shows that the average resonance frequencies of the modes increases slightly and the average bandwidths of the modes decreases with the increase in the waviness of the wires. The simple example in Fig. 4 – Fig. 5 shows the usefulness of the CMA in predicting the general trends of coupling to wires with arbitrary shapes.

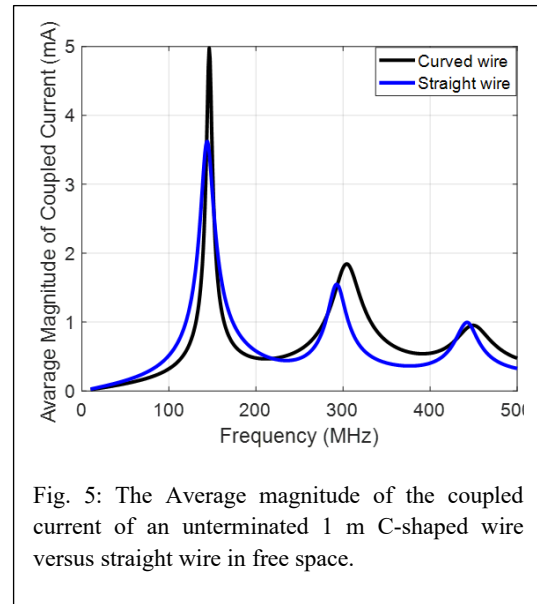


Fig. 5: The Average magnitude of the coupled current of an unterminated 1 m C-shaped wire versus straight wire in free space.

Use CMA to optimize coupling to an unterminated wire

To clarify the advantages of the CMA, we studied a simple but novel electromagnetic coupling problem. In this problem, the object of interest is a single perfectly conducting straight wire and the goal is to identify the optimum electromagnetic excitation to induce a specific current profile on this wire. The straight wire is a highly simplistic structure, but the optimization can be extended

U // Distribution A

to a more practical distribution of wires in a realistic environment. The goal of the optimization is to calculate, in a computationally efficient manner, the optimum: (i) frequencies, (ii) amplitudes, and (iii) phases of the electromagnetic waves needed to generate the required current distributions on the wire.

We will assume that the incident plane waves are always incident at an angle of 45° with respect to the wire as shown in Fig. 6. This angle can arise in a practical configuration where the location of the antenna relative to the wire causes the incident waves to fall on the wire at an angle of 45° . The dimensions of the wire are: length $L = 20$ cm and radius $a = 0.25$ mm. Our optimization

test will be to find the optimum electromagnetic excitation that maximizes the current on the wire segment confined between the 2.4 cm and 6.9 cm and minimize the current elsewhere on the wire. Therefore, the ideal current profile, J_{opt} , is shown in Fig. 7.

The CMA provides the fundamental modes of the structure. That is, it will calculate the only current modes that can be supported by the structure. Therefore, to generate the current profile in Fig. 7 in an efficient manner, the first step is to decompose the desired current as a summation of the fundamental modes of the wire. For a straight wire, the current of the first mode can be approximated as $\sin(\pi x/L)$, the current of the second mode can be approximated by $\sin(2\pi x/L)$, and the third mode can be approximated by $\sin(3\pi x/L)$. Higher order modes also show similar behavior, and they can also be approximated by $\sin(n\pi x/L)$ [1]. The advantage of the sinusoidal approximation is that we can leverage the well-established Fourier Sine Series analysis to decompose the desired current distribution in Fig. 7 as a weighted sum of the modes. If the wiring configuration is not as simple as the single wire in Fig. 6, the currents can be more complicated than the sinusoidal approximations. In this case, the decomposition of the desired current into a

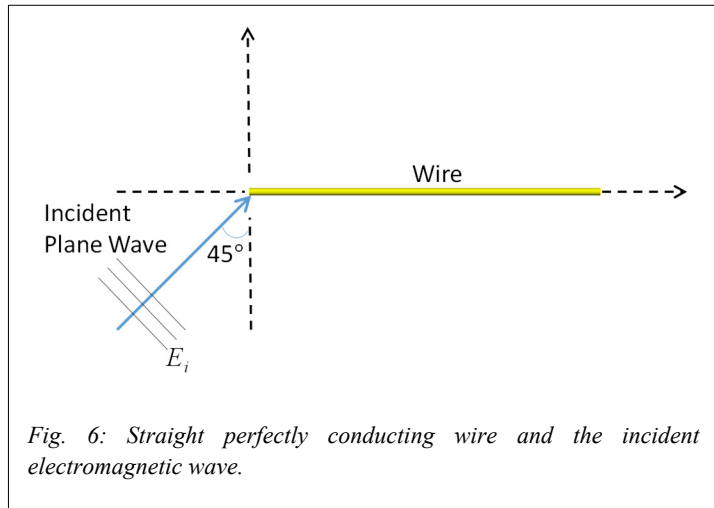


Fig. 6: Straight perfectly conducting wire and the incident electromagnetic wave.

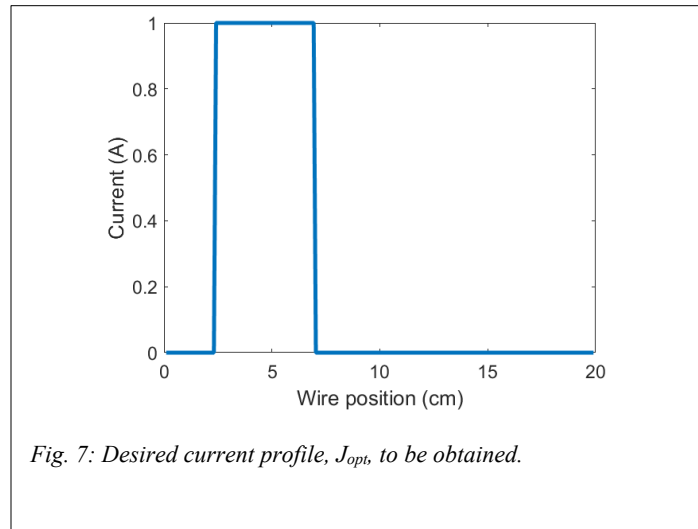


Fig. 7: Desired current profile, J_{opt} , to be obtained.

weighted summation of the modes can be calculated using similar expressions based on CMA theory [1].

A superposition of an infinite number of modes is necessary to capture the exact shape of J_{opt} . However, if a sufficiently high enough number of modes is included, a satisfactory approximation of J_{opt} can be achieved. The challenge with using higher order modes, is that they are only significant at higher frequencies as will be detailed later in this section. Therefore, given a certain maximum frequency, as prescribed by the available antenna system or other practical considerations, CMA can identify the number of modes that are significant and therefore CMA can identify the number of terms that can be used in the summation in (1a). Fig. 8a shows the Fourier Series decomposition of J_{opt} using the first 3 modes whereas Fig. 8b shows the Fourier Series decomposition of J_{opt} using the first 20 modes. Clearly, using 20 modes provides a better representation of the square-shaped J_{opt} . However, to excite 20 modes on the wire will require an incident pulse with $\sim 20/3$ larger bandwidth than the 3 modes incident pulse.

To simplify the mathematical analysis, we will focus on the 3 modes representation of J_{opt} . The goal is to use CMA to calculate the optimum excitation that will excite the first three modes with coefficients/amplitudes matching the desired values in Fig. 9. Fig. 10 shows the magnitude of the modal significance $|MS_n|$ of the first 3 modes versus frequency. The graph shows that up to 0.7175 GHz only Mode 1 is significant and therefore this is the only mode that can be excited on the wire regardless of the incident electromagnetic excitation. In the frequency band up to 1.46 GHz, only Mode 1 and Mode 2 are significant and those are the two only modes that can be excited in this frequency range. Higher order modes will only be significant at higher frequencies and they will require incident wave with higher frequencies to be excited. Our goal was to excite the first three modes with weighted coefficients, b_1 , b_2 , and b_3 , matching the optimum values in Fig. 9b. Since three coefficients are available, we need a system of three equations to deterministically generate these optimum values. Therefore, we will opt for an excitation composed of three incident plane waves at three different frequencies. Each plane wave will have an electric field with a different

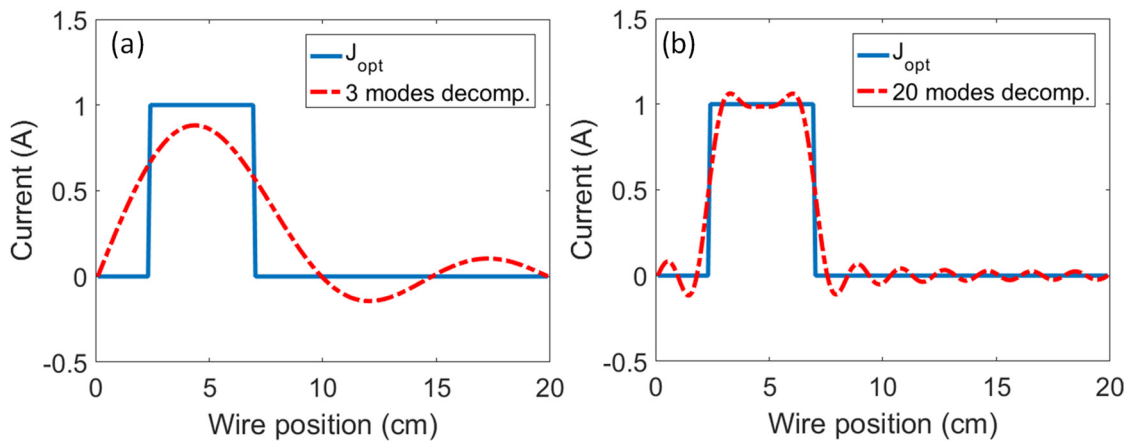


Fig. 8: Fourier series decomposition of the desired current J_{opt} in terms of (a) 3 modes and (b) 20 modes

amplitude and phase $A_i e^{j\phi_i}$. The system of equations can be solved to calculate the desired unknowns $\{A_1, \phi_1\}$, $\{A_2, \phi_2\}$, and $\{A_3, \phi_3\}$. The resulting current on the wire due to these three plane waves can be shown in Fig. 11 which compares the desired J_{opt} with the achieved CMA optimized current. It is clear that the CMA optimized current shows excellent agreement with the 3 modes decomposition of J_{opt} shown in Fig. 9a and it is a good approximation to the desired

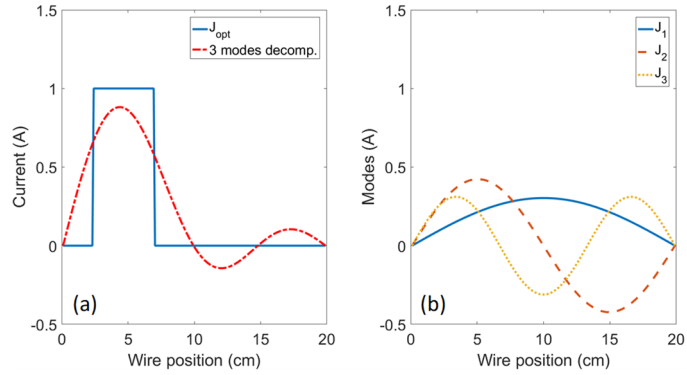


Fig. 9: (a) Desired current J_{opt} and (b) the weighted three modes.

J_{opt} . A closer match to J_{opt} can be achieved by additional modes. It is important to emphasize that the optimization procedure outlined above comes at no additional computational cost. That is, this is a deterministic optimization and requires no trial and error or computationally expensive iterations.

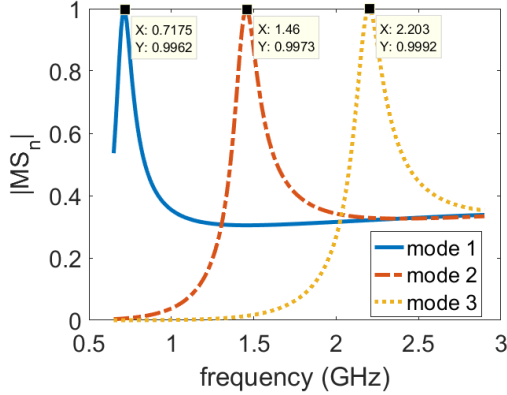


Fig. 10: Modal Significance of the first 3 modes of the straight wire

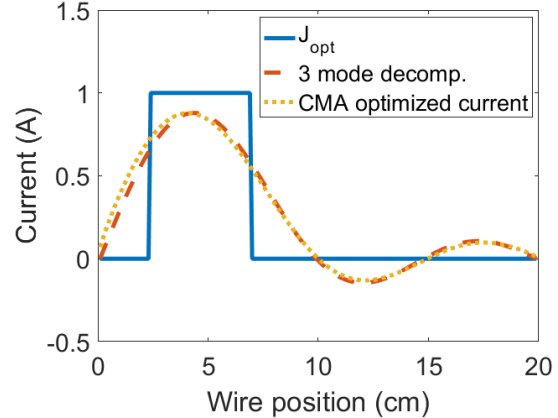


Fig. 11: CMA optimized current versus J_{opt}

Experimental Verification of CMA Predictions

Numerous simulations and measurements are typically required to quantify the electromagnetic interference statistics of a device due to radiation at different angles of incidence, polarization, and frequency. CMA has the potential to reduce the number of necessary measurements and simulations by revealing the device’s modal behavior, which allows the prediction of the variations in the

interfering current. To validate the CMA predictions, multiple wire-like DUTs were placed inside an EMCO 5317 GTEM excited by a Rohde & Schwarz ZVA 24 vector network analyzer (VNA). The wave propagates from the narrow end to the wide side of the GTEM, where pyramidal foam absorbers are placed to absorb the incident radiation and prevent reflections. The BCP-512 Broadband Current Probe with a frequency range of 1 MHz – 1 GHz was positioned at different points of interest to sample the local coupled current. The output of the current probe is connected to the second port of the VNA. The VNA S_{21} measurements are then collected and transformed into the actual coupled current values using the impedance response of the probe.

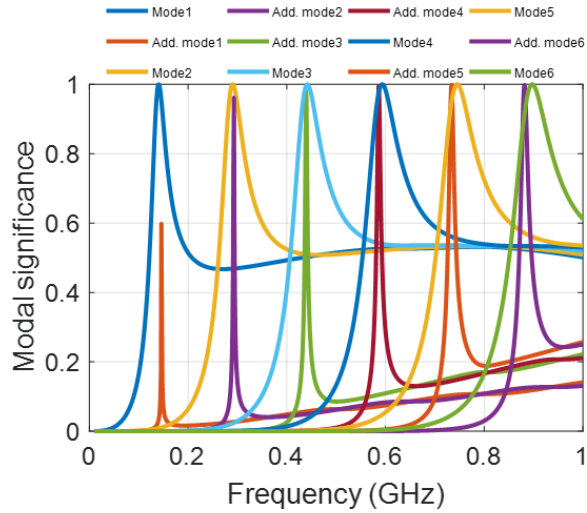


Fig. 12: Modal significance of the unterminated wire-pair in Fig. 1a.

Fig. 12 shows the modal significance of an unterminated wire pair. Within a specific frequency range, the modes of the wire pair are double that of a single wire of the same dimensions. That is, each mode of a single wire splits into two modes when the wire is placed in a pair. Fig. 13 shows that the first Mode of a single wire splits into two modes for a wire-pair: in-phase Mode 1 and out-of-phase Additional Mode 1. Fig. 13 shows that for Mode 1 and Additional Mode 1, both wires carry currents that have a $\sin(\pi x)$ behavior where x is the normalized length of each wire. However, for Mode 1, the currents in the two wires are in phase, whereas for Additional Mode 1, the currents in the two wires are 180° out of phase. Notably, the additional out-of-phase modes have narrow bandwidths as shown in Fig. 12. CMA predicts that at normal incidence in the azimuth and zenith directions, ($\theta = 0^\circ$ and $\phi = 0^\circ$), the additional out-of-phase modes cannot be excited. However, for oblique

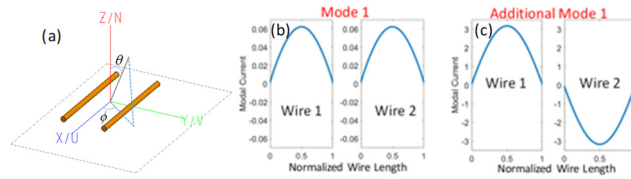


Fig. 13. (a) A wire pair showing two straight wires of radius a , length L , and inter-wire separation d , (b) The current distribution of in-phase Mode 1 and (c) the out-of-phase Additional Mode 1.

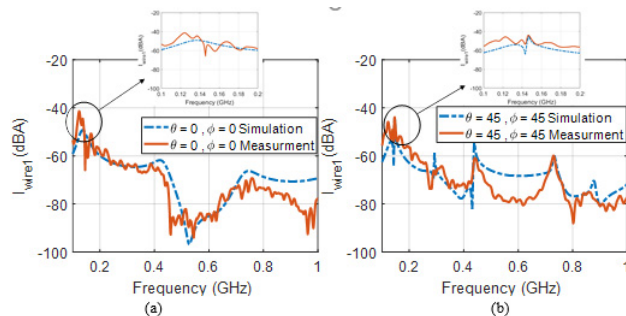


Fig. 14. The coupled current at the center of wire 1 for two different incident field angles: a) normal incidence (b) oblique incidence.

incidence, for example ($\theta = 45^\circ$ and $\phi = 45^\circ$), the additional modes can be excited and their expression in the total current of the wires is predicted to be clear due to their sharp resonances. We tested these predictions both numerically and experimentally for multiple DUTs and the results will be discussed in the following section. In summary, Fig. 12 and Fig. 13 show the versatility of CMA in predicting the coupling current at different values of θ and ϕ without the need to explicitly measure the current at these values. Moreover, we demonstrated that CMA could guide experimental measurements by predicting the frequencies and excitations where RF coupling is maximum.

Fig. 14 shows the total coupled current to the center of one of the two wires in Fig. 1a at normal incidence ($\theta = 0^\circ$ and $\phi = 0^\circ$) and at oblique incidence ($\theta = 45^\circ$ and $\phi = 45^\circ$). Both cases show excellent agreement between the simulations and the experimental measurements. Moreover, in agreement with the CMA predictions, the case of oblique incidence shows additional sharp resonances, e.g. at 0.3 GHz, 0.45 GHz, and 0.7 GHz, which correspond to the additional modes in Fig. 12. Due to this narrow bandwidth, an unguided experiment or simulation of this DUT might miss the effects of this mode by not selecting the enough frequency points in the region where it is significant or by not selecting the correct angles of incidence where this mode can be expressed in the total coupled current.

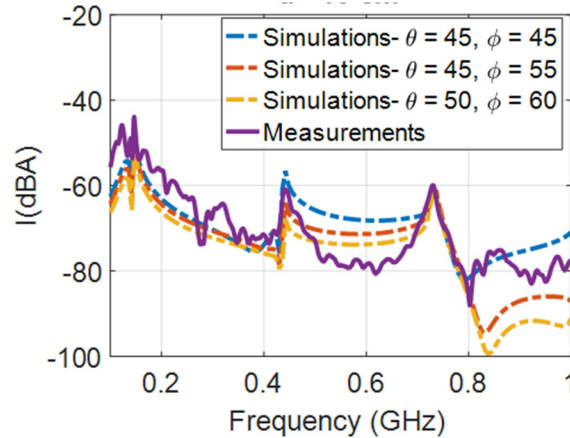


Fig. 15. Sensitivity analysis of the coupled current to variations in θ and ϕ .

For the oblique incidence case, there is a slight discrepancy between the simulated and measured current in the central frequency range between 0.4 GHz and 0.7 GHz. To investigate this discrepancy, we repeated the simulations for θ and ϕ values that are slightly different from the exact value of 45 degrees and plotted the results in Fig. 15. The central region of the coupled current became much closer to the measurements and the other regions of the coupled current stayed insensitive to this small θ and ϕ variations as shown in Fig. 15. This indicates that there was a slight misalignment in the direction of the incident field with respect to the DUT. We hypothesize that this misalignment was caused by a shift in the DUT orientation or by the slight inhomogeneity of the electric field inside the TEM cell itself. Moreover, this analysis shows that some frequency regions are more sensitive to the orientation of the DUT than others, and therefore will require a finer step size in varying θ and ϕ , which can help guide the RF coupling analysis and experimental measurements.

CMA of RF Coupling to load-terminated wire systems:

In practical configurations, wire systems are terminated with linear or nonlinear loads. Therefore, in this section, we discuss the CMA predictions of coupling to terminated wire systems. Fig. 16

U // Distribution A

shows a 1 m wire, 3 mm in radius, and at the height of 0.1 m above an infinite ground plane. The wire is terminated at both of its ends by 50Ω loads labeled as Load 1 and Load 2, respectively. Moreover, a third 50Ω load, Load 3, is attached to the middle of the wire. In spite of the simplicity of the configuration in Fig. 16, it has practical relevance in a wide range of studies [7] – [9]. The goal is to show how CMA can be used to simplify the coupling analysis to specific loads in a wire system similar to what is shown in Fig. 16.

The CMA of the wire configuration in Fig. 16 is performed using the commercial electromagnetic solver FEKO [10]. The components of the CMA are threefold: (i) the modal significance spectrum (Fig. 17), (ii) the modal current distribution (Fig. 18), and (iii) the modal fields also termed the radiation characteristics of each mode (Fig. 19). In the context of electromagnetic interference, the modes represent all possible pathways for the external electromagnetic radiation to couple to the wire configuration in Fig. 16. The modal completely independent of the external excitation. The modal fields represent the coupling between the incident field and the modes. That is, the modal field patterns can be defined as the map of the electric field directions that minimize/maximize the coupling between the incident radiation and a particular mode.

CMA provides the current distribution of the fundamental modes of the structure, allowing the prediction of the response at different wire locations. For example, Fig. 18 shows that only the even modes, Modes 2, 4 and 6, have nonzero currents at the middle of the wire. Thus, RF coupling to the middle load, Load 3, is determined by the even modes and is entirely independent of the odd modes.

Starting with Mode 2, Fig. 19 shows that Mode 2 is more efficiently excited by a plane wave incident at an angle of $\theta = 90^\circ$ and $\Phi = 45^\circ$ (the green curve). Fig. 17 shows that Mode 2 resonates

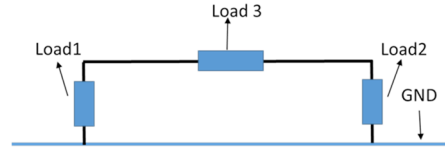


Fig. 16. Terminated wire above perfectly conducting ground plane.

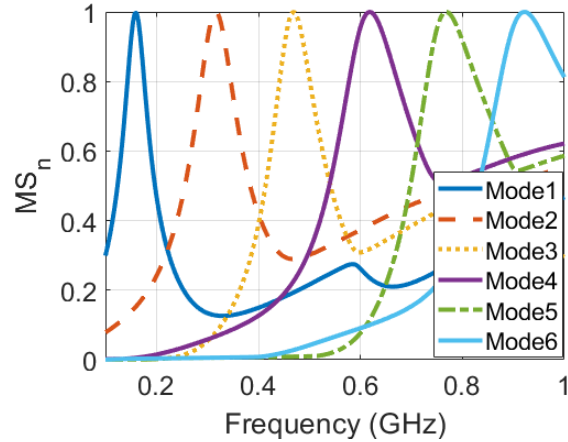


Fig. 17. Modal Significance of the wire configuration shown in Fig. 1.

current distribution and the modal significance are

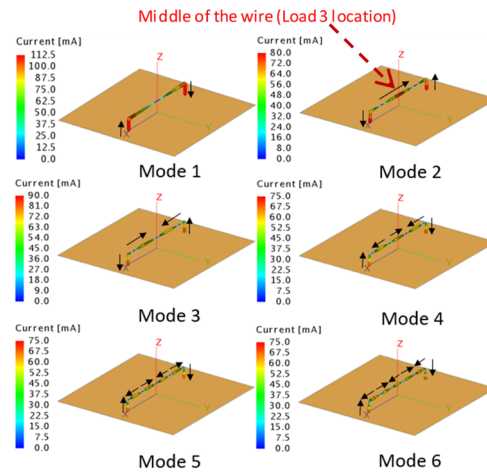


Fig. 18. Modal currents of the first 6 modes of the wire configuration.

at 0.3 GHz. Therefore, Mode 2 should be strongly expressed in the coupled current to Load 3 at 0.3 GHz for an incident plane wave at angles of incidence $\theta = 90^\circ$ and $\Phi = 45^\circ$. On the other hand, Fig. 17 shows that Mode 6 resonates at 0.9 GHz and Fig. 19 shows that Mode 6 can be most efficiently excited at angles of incidence $\theta = 50^\circ$ and $\Phi = 0^\circ$. Therefore, at angles of incidence $\theta = 50^\circ$ and $\Phi = 0^\circ$ maximum coupling should occur at 0.9 GHz which is the resonance frequency of Mode 6.

To test this hypothesis, Fig. 20 shows the coupled current to Load 3 for two different excitations. The current coupled to Load 3 is maximum at 0.3 GHz when $\theta = 90^\circ$ and $\Phi = 45^\circ$, due to the strong excitation of Mode 2, and the current coupled to Load 3 is maximum at 0.9 GHz when $\theta = 50^\circ$ and $\Phi = 0^\circ$, due to the excitation of Mode 6. A similar analysis can be performed for the coupling to Load 1 and Load 2.

In summary, a simple wire configuration with three loads was studied to predict and control the coupling to each load individually at different frequencies. Characteristic Mode Analysis (CMA) was applied to identify all the modes of the structure and the possible ways to maximize/minimize coupling to each mode and thereby controlling coupling to specific loads. This study demonstrates that, for an identified and a well-characterized DUT, CMA can be used to predict the optimum frequency and angle of incidence to target a specific load in a multi-load wire system.

Big Data Acceleration of the Characteristic Mode Analysis

The implementation of CMA involves the evaluation of a large method of moments (MoM) complex impedance matrix at every frequency. In this work, we use different open-source software for the GPU acceleration of the CMA. This open-source software comprises a wide range of computer science numerical and machine learning libraries not typically used for electromagnetic applications. Specifically, we explored different Python-based libraries to optimize the computational time of the matrix operations that compose the CMA algorithm. Based on our

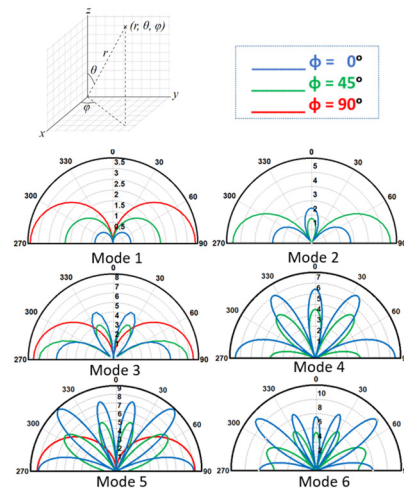


Fig. 19. Modal fields of the first 6 modes of the wire configuration shown in Fig. 16.

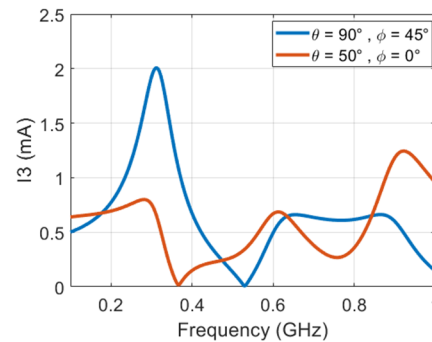


Fig. 20. Induced current on Load 3 for different field orientations.

computational experiments and optimizations, we showed that a Graphics Processing Unit (GPU) platform is able to achieve up to $16\times$ and $26\times$ speedup for the CMA processing of a single $15k\times 15k$ MoM matrix of a perfect electric conductor scatterer and a single $30k\times 30k$ MoM matrix of a dielectric scatterer, respectively. In addition to improving the processing speed of CMA, our approach provided the same accuracy as independent CMA simulations. The speedup, efficiency, and accuracy of our CMA implementation will enable the analysis of electromagnetic systems much larger than what was previously possible at a fraction of the computational time.

Coupling to a wire system with nonlinear loads attached: An Equivalent Circuit Approach (ECA)

We started by using the ECA, shown in Fig. 1 and Fig. 2, to simple nonlinear loads connected to the simple wire system shown in Fig. 21. The equivalent circuit of the wire-system in Fig. 21 was calculated as shown in Fig. 1 and Fig. 2. For the load, we used the nonlinear Schottky diode model similar to [11]. The Schottky diode was connected to one side of a $10.5\text{ cm} \times 10.5\text{ cm}$ wire loop that has a radius of 0.25 mm , as shown in Fig. 21, and a $1\text{ M}\Omega$ load was attached to the opposite side.

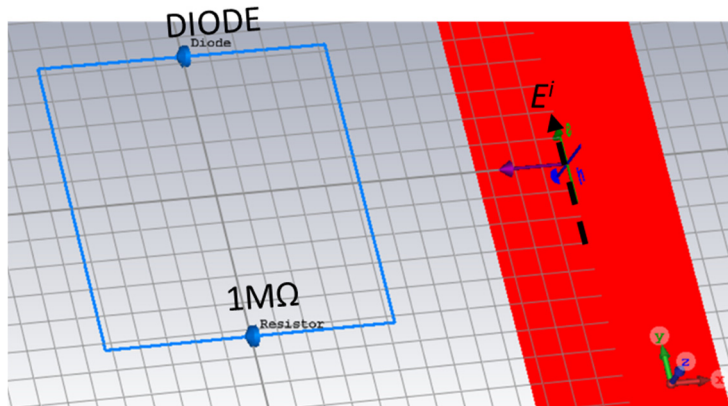


Fig. 21: Wire loop loaded by one diode and a high impedance load opposite to the diode.

U // Distribution A

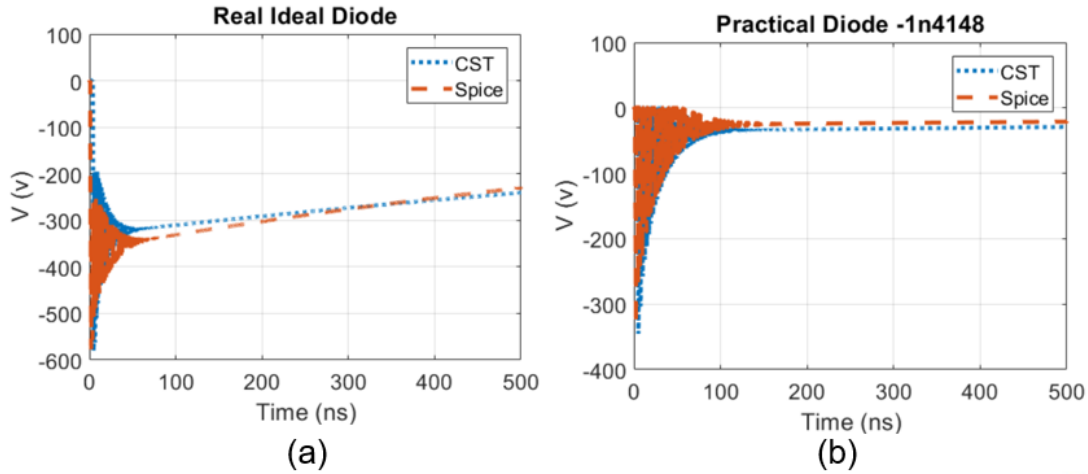


Fig. 22: Induced voltage across the nonlinear diode calculated using the full-wave solver (CST) and the Thévenin circuit approach (Spice) for (a) ideal diode. (b) practical diode (1N4148).

Typically, the properties of nonlinear devices vary significantly, even for simple components like a diode. Therefore, in Fig. 22 we studied two different diode models: (i) An ideal diode and a practical (ii) 1N4148 diode. In both cases, the diode was attached to the wiring system shown in Fig. 21. The orientation of the electric field and the magnetic field are shown by the green and the blue arrows, respectively, in Fig. 21, and for both diode models, a double-exponential pulse was used to excite the structure.

The results in Fig. 22 illustrates the validity of the approach for the ideal as well as practical diodes. More importantly, Fig. 22 shows the significant differences between the response of an ideal diode and a practical diode. An ideal diode assumes a zero resistance for forward bias and infinite resistance for reverse bias. These assumptions cause a sharp transient increase in the voltage across the diode, up to ~ -600 V, as shown in Fig. 22a. Moreover, it takes a long time for the voltage across the diode to discharge back to zero. A practical diode will, however, have a finite reverse resistance and a parallel junction capacitance. Therefore, the maximum transient voltage for a 1N4148 diode is only -350 V versus -600 V for an ideal diode. After 500 ns, the voltage across a 1N4148 diode is less than 30 V, as shown in Fig. 22b, whereas for an ideal diode, the voltage perseveres to more than 230 V, as shown in Fig. 22a. The difference in the maximum voltage and in the buildup voltage may affect the operation status of the device. Therefore, the accurate equivalent circuit of nonlinear devices needs to be incorporated in RF coupling studies and not just the ideal representation.

Next, we will summarize the effect of different excitation pulses on the coupling to the loop configuration shown in Fig. 21. The configuration in Fig. 21 is a $10.5 \text{ cm} \times 10.5 \text{ cm}$ loop with a $1 \text{ M}\Omega$ load connected at one side of the loop and a nonlinear Schottky diode connected on the opposite side of the $1 \text{ M}\Omega$ load [1]. The electric field direction is perpendicular to the loop edge

U // Distribution A

that carries the diode. The input impedance of the loop, as seen from the diode port, is shown in Fig. 23.

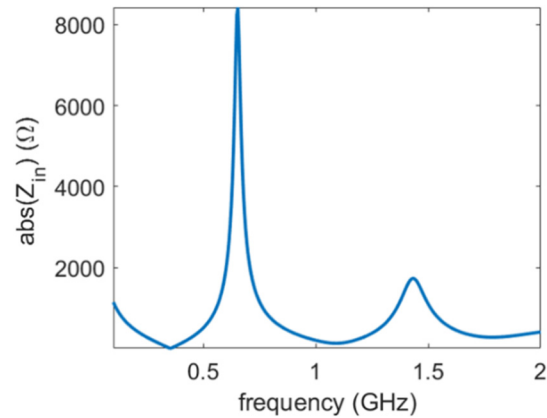


Fig. 23: Input impedance of the loop seen from the diode port in the loop shown in Fig.21.

The six pulses shown in Fig. 24 are used to excite the loop configuration shown in Fig. 21. The pulses in Fig. 24 were calculated using analytical formulas, that is, they do not correspond to a specific source, but they differ in duration, shape, rise time, and the corresponding frequency content. A Pulse Repetition Frequency (PRF) of 1 MHz is assigned to all six pulses. We performed the Fourier Transform of the incident pulses to study their frequency content and compared the frequency content of each pulse with the input impedance/admittance Z_{in}/Y_{in} of the loop. The voltage coupled to the wire configuration is divided between the input impedance, Z_{in} , of the wire configuration itself, and the impedance of the load Z_L , as shown in Fig. 1. Therefore, the lower the magnitude of Z_{in} , the higher the portion of the voltage that goes to the load according to the voltage divider concept. That is, the frequencies where Z_{in} is minimum, i.e., Y_{in} is maximum, are the frequencies where the coupling to the load, Z_L , will be maximum.

U // Distribution A

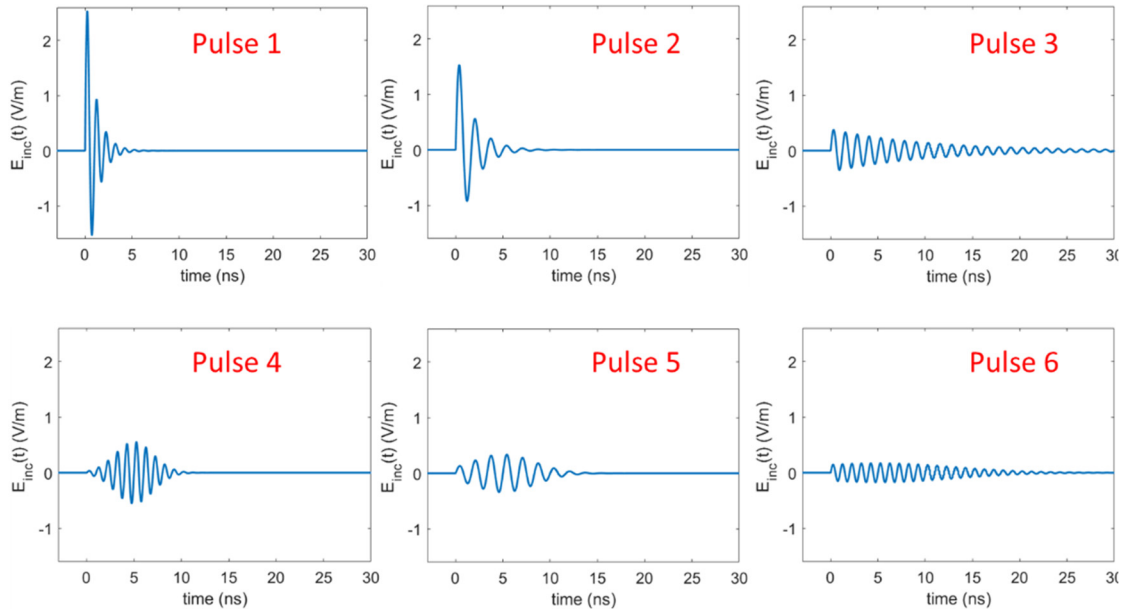


Fig. 24: 6 different pulses used to excite the loop configuration shown in Fig. 21.

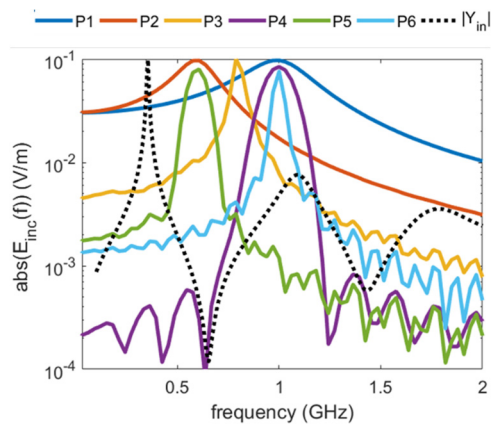


Fig. 25: comparison between the spectrum content of the 6 excitation pulses and the input admittance of the loop.

U // Distribution A

We performed the Fourier transform of the six pulses in Fig. 24 and the frequency spectrum of each pulse is plotted in Fig. 25 alongside the input admittance, Y_{in} , of the wire configuration in Fig. 21. The pulses which have the largest magnitude at the resonance frequencies of Y_{in} are predicted to couple the maximum voltage to the load. For example, focusing on the main resonance of Y_{in} in Fig 25, 0.35 GHz, we can predict that Pulse 2 and then Pulse 1 will generate the largest voltage across the diode. Fig. 26 shows the induced voltage across the diode for the 6 excitation pulses shown in Fig. 24. Fig. 26 confirms the predictions that Pulse 2 will couple the largest voltage to the diode followed by Pulse 1. This predictive capability shows the advantage of the equivalent circuit approach in providing additional insight into the RF coupling process to a particular wire configuration.

Another important feature of the results in Fig. 26 is the voltage buildup. Note that the polarity of the voltage shown in Fig. 26 depends on which port of the diode's two terminals is designated as positive and which is designated as negative. Therefore, we will focus mainly on the magnitude of the voltage shown in Fig. 26. If the induced voltage after 3000 ns is compared for the 6 pulses, Pulse 2 will still have a significant voltage across the diode, followed by Pulse 1 and then Pulse 5. The other three pulses will die out fast and have no voltage build up after the 3000 ns period. The analysis in Fig. 26 shows that different pulses will result in different maximum transient voltages and different voltage buildup. These voltage differences can be correlated consequently with varying effects on the nonlinear components.

The predictive capability of the equivalent circuit approach motivated us to apply the same concept to three practical pulses generated by actual sources. The three pulses are shown in Fig. 27. A train of pulses is applied with 1 MHz PRF to excite the loop structure. The frequency contents of the three pulses are compared with the input admittance of the loop in Fig. 28.

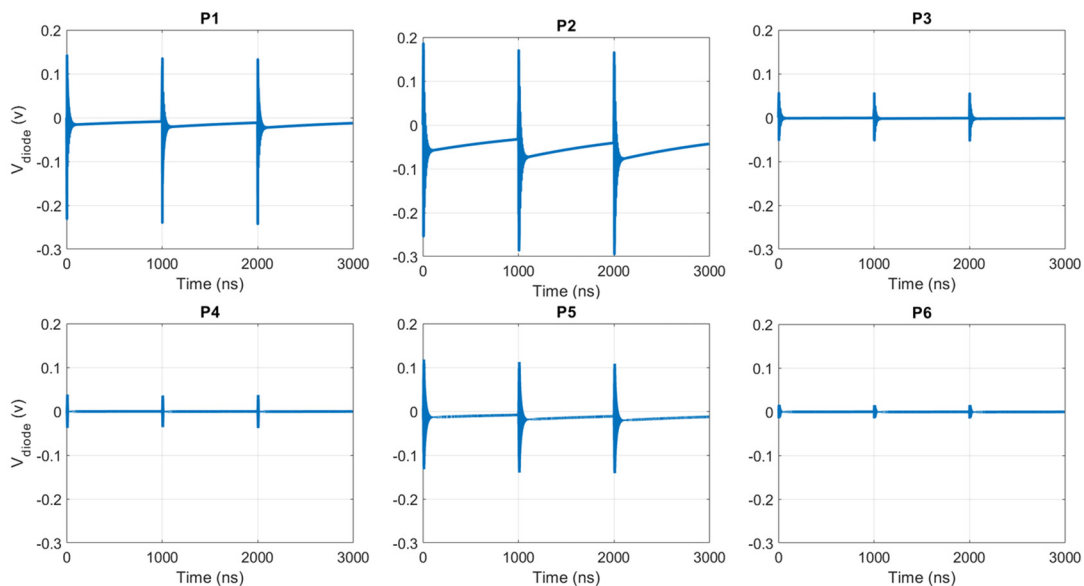


Fig. 26: The induced voltage across the diode in Fig.14 for the 6 different pulses in Fig.17 used to excite the loop.

U // Distribution A

Focusing again on the resonance frequency of Y_{in} , 0.35 GHz, we can predict from Fig. 28 that Pulse 3, the yellow curve, will couple the highest voltage to the diode because it has the highest magnitude at this frequency. Pulse 2, the red curve, will result in the lowest induced voltage across the diode since it has the lowest value at 0.35 GHz. The induced voltage across the diode was then calculated

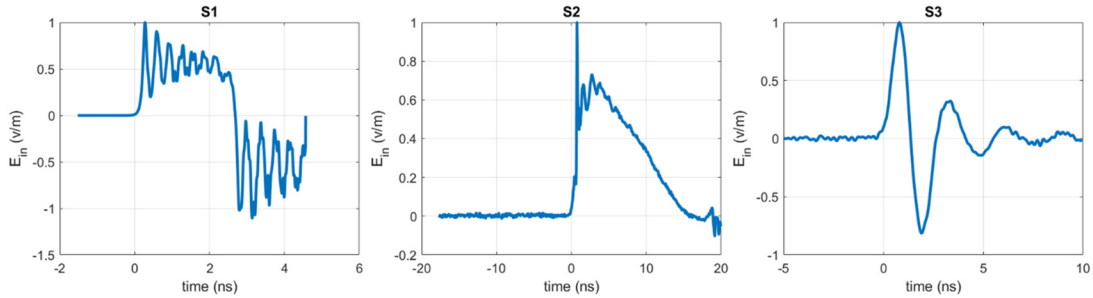


Fig. 27: the three sponsor pulses used to excite the loop configuration shown in Fig.14.

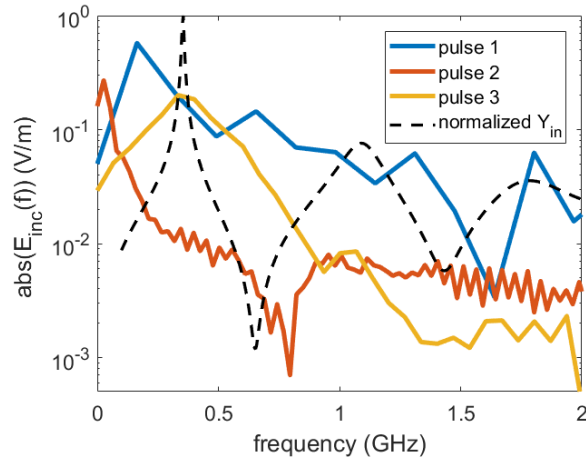


Fig. 28: comparison between the spectrum content of the sponsor three excitation pulses and the input admittance of the loop.

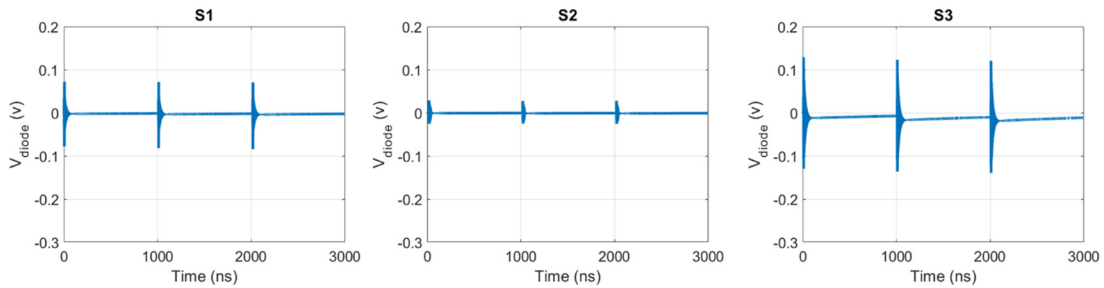


Fig. 29: The induced voltage across the diode in Fig. 21 for the three sponsor pulses in Fig. 27.

using a full-wave electromagnetic solver and presented in Fig. 29 validating our predictions. The computational experiments presented in this section, prove the validity of the equivalent circuit approach to predict the optimum pulse, out of a set of pulses, which couples the maximum voltage across a nonlinear device connected to a wire system.

Equivalent Circuit Approach (ECA) Prediction of Coupling to a Wiring System

Consider the configuration in Fig. 30 to test the voltage buildup across a nonlinear electronic component connected to a wire/trace system. The same configuration was studied computationally using CST full-wave simulations and the Equivalent Circuit Approach (ECA). We highlight the predictive capability of the ECA to identify the optimum incident waveform to create the desired effect on the nonlinear electronic component of interest. The configuration consists of a square trace printed on an FR4 substrate connecting a 1 M Ω resistor and an RB886CST2R Schottky diode in Fig. 30a similar to [3]. The thickness of the FR4 substrate was 1.7 mm, and its dielectric substrate had a relative dielectric permittivity $\epsilon_r = 4.8$ and a loss tangent of 0.017. The square trace measures 10.5 cm by 10.5 cm, and the thickness of the trace was 1 mm. We can predict the waveform properties that will require the least amount of incident power to maximize the coupling to the diode. The steps of the ECA predictive capabilities are:

- 1- Remove the diode from the circuit in Fig. 30a and calculate the input impedance seen at the port where the diode is to be connected. The input impedance, Z_{in} , should be calculated over the frequency bandwidth of interest using a full-wave electromagnetic solver. Fig. 30b shows the input impedance of the system in Fig. 30a calculated using the full-wave solver FEKO.

- 2- Represent the input impedance calculated in (1) with an equivalent circuit composed of a series of RLC networks. One RLC series is needed for every resonance in the input impedance, Z_{in} , over the frequency range of interest. As the frequency range of interest increases, additional RLC or different circuit representations needs to be added. But it is important to emphasize that this step is not an approximation. No loss in accuracy will be experienced as long as sufficient circuit elements are used to match the input impedance, Z_{in} , obtained from the full-wave solver. Fig. 30c shows the

equivalent circuit and Fig. 30b shows the close agreement achieved between the impedance calculated from the full-wave solver and the input impedance calculated from the equivalent RLC circuit.

3- Use the full-wave electromagnetic solver to calculate the open-circuit voltage at the port where the diode is to be connected versus frequency. This open-circuit voltage will be calculated due to a waveform at a particular incident direction. The open-circuit voltage due to different incident directions can be efficiently calculated using the Characteristic Mode Analysis as discussed in the previous sections. Fig. 30d shows the open-circuit voltage versus frequency for the system in Fig. 30a, and it shows that not all frequencies couple equally to the trace system.

4- The voltage across the electronic component, the RB886CST2R Schottky diode, can be expressed using the circuit voltage divider as $(V_{oc}Z_L)/(Z_L+Z_{in})$, which can be readily calculated using a SPICE solver since it is affected by the electronic component, in this example, the diode. Fig. 30e shows this factor which acts as the transfer function from the incident wave to the diode.

5- The transfer function obtained from step 4 shown in Fig. 30e, provides a plethora of physical insight into the coupling problem. The resonance frequencies in Fig. 30e are the ideal frequencies to couple energy into the electronic component, which is the diode. The main resonance is achieved at 0.477 GHz. Therefore, exciting the system with a pulse centered around this frequency will couple more than any other pulse centered around a different

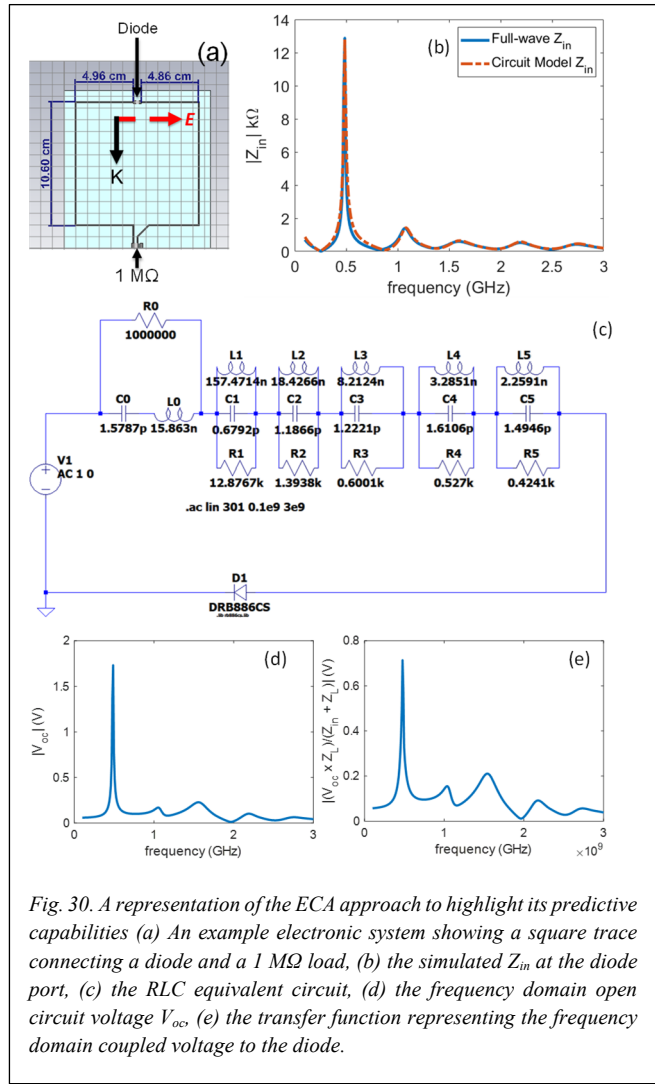


Fig. 30. A representation of the ECA approach to highlight its predictive capabilities (a) An example electronic system showing a square trace connecting a diode and a 1 MΩ load, (b) the simulated Z_{in} at the diode port, (c) the RLC equivalent circuit, (d) the frequency domain open circuit voltage V_{oc} , (e) the transfer function representing the frequency domain coupled voltage to the diode.

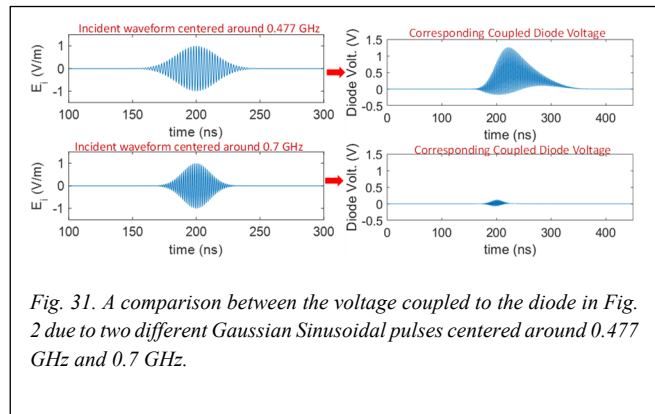


Fig. 31. A comparison between the voltage coupled to the diode in Fig. 2 due to two different Gaussian Sinusoidal pulses centered around 0.477 GHz and 0.7 GHz.

frequency. Fig. 31 shows two different incident waveforms, each a Gaussian Sinusoidal pulse. The first pulse is centered around 0.477 GHz, and the second pulse is centered around 0.7 GHz. Both pulses had the same amplitude of 1 V/m and a bandwidth of 5%. Fig. 31 shows the coupled voltage across the diode due to the two different incident waveforms and clearly confirms the ECA predictions that the 0.477 GHz Gaussian sinusoidal pulse will maximize coupling. The maximum voltage coupled to the diode for the 0.477 GHz Gaussian sinusoidal pulse was 1.26 V, whereas it was 0.118 V for the 0.7 GHz Gaussian sinusoidal pulse. For the 0.7 GHz, to induce the same maximum voltage on the diode, its incident power needs to be increased by at least 20 dB. Therefore, the previous example show that the ECA can reduce the power required to create the desired disruptive effect on the diode by at least 20 dB just by identifying the optimum frequency.

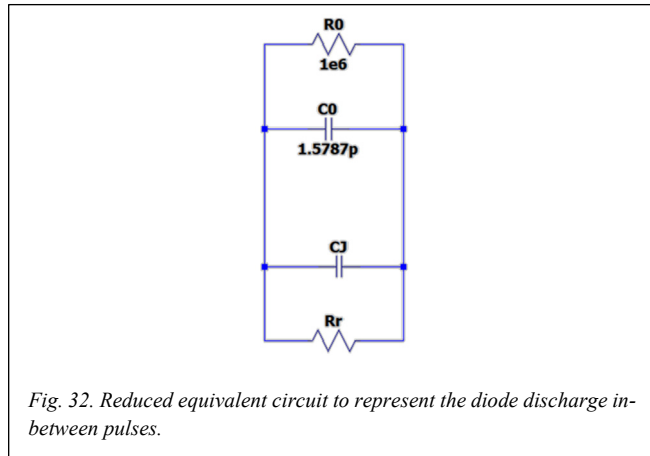


Fig. 32. Reduced equivalent circuit to represent the diode discharge in-between pulses.

The ECA can also predict the minimum Pulse Repetition Frequency (PRF) of the incident waveform to create the desired effect.

In between pulses, the voltage buildup across the diode discharges. The ECA can help predict how fast the diode discharge will be, i.e, the time constant of the discharge process, such that we can make sure that the next pulse will arrive soon enough before the voltage across the diode drops significantly. That is, by knowing the discharge time constant of the diode, τ , we can predict the minimum PRF to cause the voltage buildup across the diode to continue to increase.

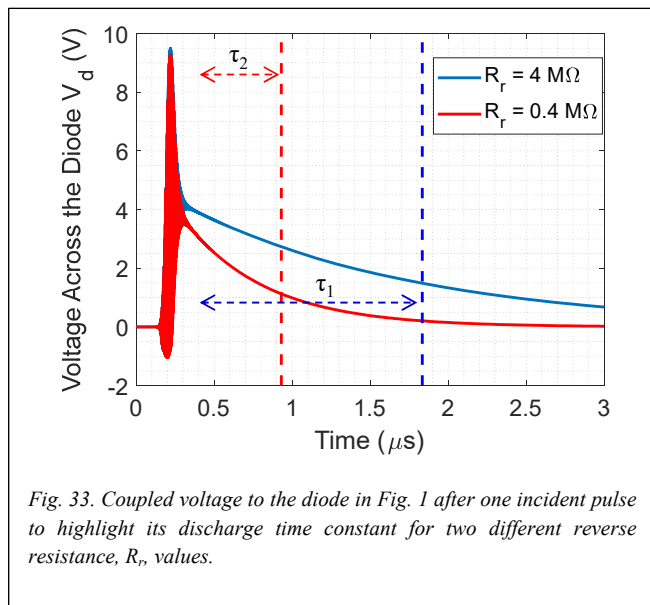


Fig. 33. Coupled voltage to the diode in Fig. 1 after one incident pulse to highlight its discharge time constant for two different reverse resistance, R_r , values.

In between pulses, the incident field drops to zero, and therefore, we can remove the voltage source in Fig. 30c [11]. All the inductors in Fig. 30c can also be replaced with a short circuit during the discharge phase [11]. Therefore, the equivalent circuit can be reduced into the 4 components shown in Fig. 32. The C_j and R_r components represent the junction capacitance and the reverse resistance of the diode, respectively. The C_0 and R_0 components are exactly the same as the ones in Fig. 30c and they physically represent the DC or the low-frequency limit of the resistance and capacitance of the square trace to which the diode is connected. Therefore, C_0 and R_0 can easily be measured

U // Distribution A

or calculated for a complex wire system using low-frequency techniques. The reduced equivalent circuit in Fig. 32 is much simpler than the one in Fig. 30c and yet completely quantifies the discharge of the diode. For example, the time constant of the discharge τ can be expressed using the following simple expression [11]:

$$\tau = (C_0 + C_J) \left(\frac{R_r R_0}{R_r + R_0} \right) \quad (1)$$

To clarify this predictive capability, we repeated the simulation in Fig. 30 but we boosted the amplitude of the pulse to 10 V/m to clarify the discharge process. Fig. 33 shows the discharge of the diode after one pulse for two different values for the reverse resistance of the diode $R_r = 4 \text{ M}\Omega$ and $R_r = 0.4 \text{ M}\Omega$. For both cases, a diode junction capacitance $C_J = 0.28 \text{ pF}$ was used. As expected, the diode discharges slower for the larger R_r value since it leads to a larger time constant according to Equation 1. We measured the time constant from the simulations highlighted in Fig. 33 and found that for $R_r = 4 \text{ M}\Omega$, $\tau_1 = 1.45 \text{ }\mu\text{s}$, and that for $R_r = 0.4 \text{ M}\Omega$, $\tau_2 = 0.53 \text{ }\mu\text{s}$, in perfect agreement with the values achieved from Equation (1) above. To ensure that the voltage across the diode builds up with every consecutive pulse, the PRF needs to obey the following relation:

$$PRF > \frac{1}{\tau} > \frac{1}{R_r R_0} \left(\frac{R_r + R_0}{C_0 + C_J} \right) \quad (2)$$

In summary, the minimum PRF that maximizes the probability of effect by ensuring that the voltage across the diode builds up with every consecutive pulse can be predicted using the ECA as follows:

- 1- Identify the junction capacitance and reverse resistance of the diode, C_J and R_r , by direct measurements or from the diode's datasheet
- 2- Measure, simulate, or calculate the equivalent resistance, R_0 , and capacitance, C_0 , of the wiring system connected to the diode at the low-frequency limit.
- 3- Set the minimum PRF according to (2).

Experimental Validations of the ECA Predictions

We developed the experimental setup in Fig. 34 to test the voltage buildup across the configuration in Fig. 30 that was studied computationally using the Equivalent Circuit Approach (ECA). The goal is to correlate the voltage buildup with any effects caused by the incident pulsed waveforms on the diode. The diode was soldered to a square wire loop at one end, and the other end of the wire loop was attached via a coaxial cable to an oscilloscope. The oscilloscope's input impedance was varied to create different effective impedances, through the coaxial cable, to the wire loop. The GTEM was excited by a waveform generator followed by an amplifier to boost the incident field to the desired level. In the experiments below, the waveform generator was programmed to generate a Gaussian Sinusoidal pulse centered around 777 MHz with a 10% bandwidth. We varied the electric field amplitude over a range that varied from 100 V/m to 1600 V/m and the Pulse Repetition Frequency (PRF) from 1 kHz to 2.5 MHz. This exhaustive parameter scan aims to identify the

U // Distribution A

waveform properties that will cause an effect on the diode, i.e. change its operating status, and correlate the effect and parameters with the voltage buildup across the diode.

Fig. 35a and Fig. 35b show the coupled voltage across the oscilloscope load, set to $1\text{ M}\Omega$, at incident electric fields of amplitudes 800 V/m and 1600 V/m , respectively. The PRF was varied from 1 kHz to 100 kHz for both incident field levels in Fig. 35. Increasing the PRF was found to increase the voltage buildup as expected. For example, PRF below 10 kHz caused insignificant voltage buildup. Once the PRF reached 50 kHz , significant voltage buildup was achieved for both incident field levels in Fig. 35. In Fig. 35a, the voltage buildup reached 5 V after $900\text{ }\mu\text{s}$ at a PRF of 50 kHz , whereas the voltage buildup reached 8.5 V after $900\text{ }\mu\text{s}$ at a PRF of 100 kHz . Of equal importance, the oscillations or “spikes” around the steady state voltage buildup increased with the PRF. In Fig. 35b, the incident field was increased to 1600 V/m and the voltage buildup reached 7.5 V after $900\text{ }\mu\text{s}$ at a PRF of 50 kHz (the dark green curve in Fig. 35b). When we increased the PRF to 100 kHz , the steady-state voltage buildup decreased to 2.5 V and did not increase as we expected (the light-

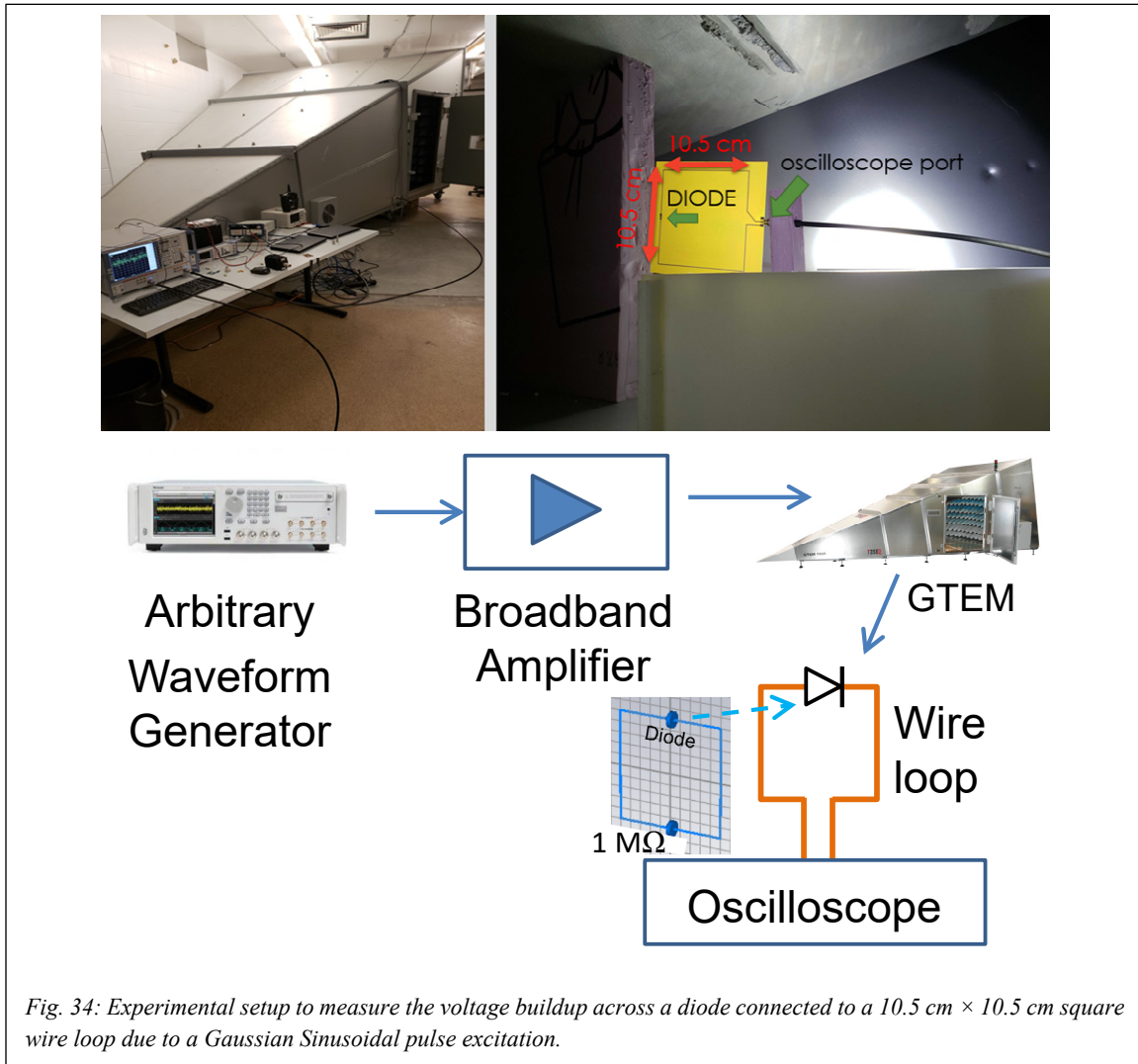


Fig. 34: Experimental setup to measure the voltage buildup across a diode connected to a $10.5\text{ cm} \times 10.5\text{ cm}$ square wire loop due to a Gaussian Sinusoidal pulse excitation.

U // Distribution A

green curve in Fig. 35b). Upon investigating the diode, we found out that it was damaged. To validate that the diode's operation status was changed, we repeated the measurement with the same trace/diode configuration, but we decreased the PRF back to 50 kHz (the yellow curve in Fig. 35b). Clearly, the dark green and the yellow curves in Fig. 35b are different even though they were recorded at the same incident field level and the same PRF, indicating that the diode's operation status was changed between the 2 measurements. Therefore, in conclusion, a PRF of 100 kHz and an incident field level of 1600 V/m were capable of changing the diode's operation status when it was connected to the square trace in Fig. 34. However, the steps employed in varying the incident field level and the PRF were coarse.

The experimental measurements were limited in the sense that we cannot measure the voltage directly across the diode and could only measure the voltage across the 1 M Ω opposite to the diode. Therefore, we used simulations to investigate the voltages and currents at different components/locations, especially across the diode. The experimental measurements in Fig. 35 show that the voltage and currents reached steady-state only beyond 800 μ s. However, a time-domain full-wave solver might take a few days to reach the saturation response for a nanosecond's excitation pulse. Moreover, to perform parametric studies to quantify the effect of different waveforms properties and the effect of various parasitic, the simulations need to be repeated multiple times, requiring a huge computational time in the order of weeks and maybe longer. However, the ECA can perform such simulations in minutes without any accuracy loss. Therefore, another advantage of the ECA is that it allows the simulation of systems and incident waveforms with relatively long Times To Effects (TTE).

We have automated the data collection of RF coupling using the experimental setup in Fig. 34. That is, to verify the ECA predictions for a particular configuration, we can now automatically expose it to hundreds of different pulses of different PRF, center frequency, pulse width whilst keeping the power per waveform constant. So far, the experimental setup can only measure the voltage across

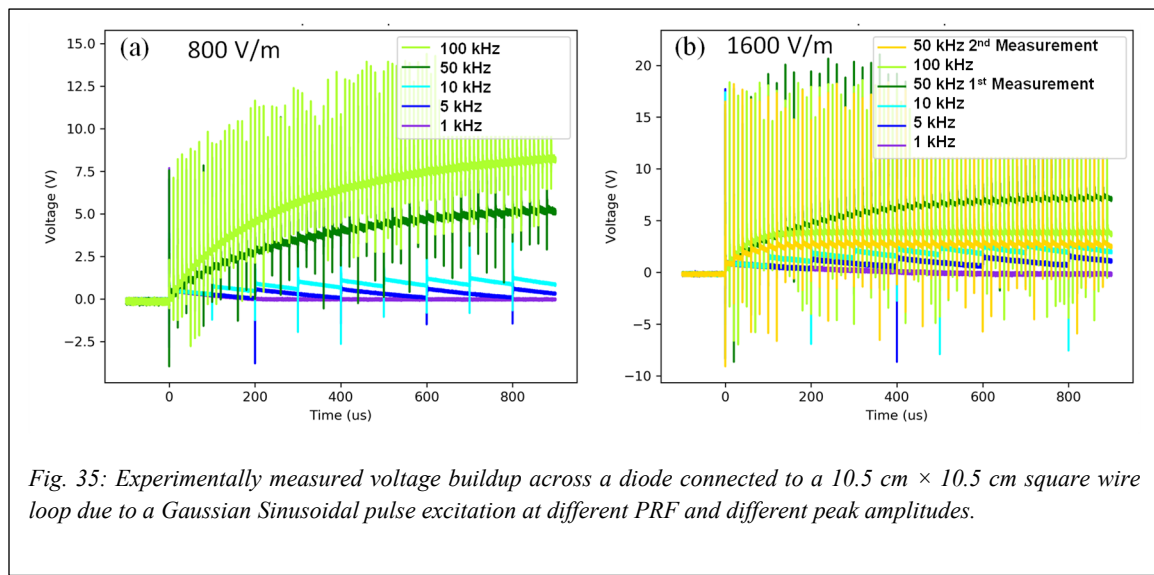


Fig. 35: Experimentally measured voltage buildup across a diode connected to a 10.5 cm \times 10.5 cm square wire loop due to a Gaussian Sinusoidal pulse excitation at different PRF and different peak amplitudes.

U // Distribution A

the 1 M Ω load and not the diode. However, the voltage across the diode and the 1 M Ω load are correlated. Examples of the test points collected from the automated data collection are shown in Fig. 36 from the same diode/trace configuration.

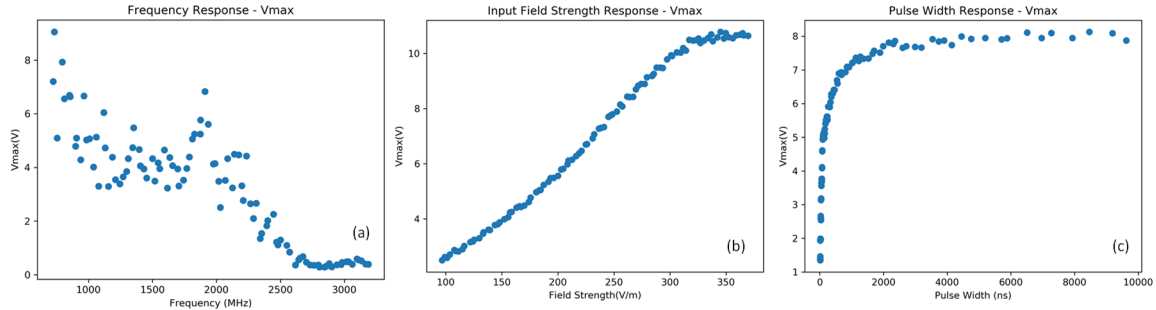


Fig. 36: Experimental RF coupling measurements from the diode trace configuration in Fig. 1a due to different incident waveforms. (a) the coupled maximum voltage versus the center frequency of the incident pulse, (b) the coupled maximum voltage versus the field strength of the incident pulse, (c) the coupled maximum voltage versus the pulse width of the incident pulse. All pulses in the previous 3 subplots had the same power.

Extending the Equivalent Circuit Approach to a Complex Wiring System: An unmanned aerial vehicle (UAV) Case Study

Sadraey *et al.* classified UAVs according to their sizes, where the size is defined as the longest dimension of the UAV [12]. For quadcopters, the size of the UAV is measured from the opposite corner motors. In this work, we studied a quadcopter 54 cm in size. We created a full-wave model of the complete UAV system with all the wires and IC components to use as a numerical platform for studying the RF coupling to the system. The MakerBot Digitizer Desktop 3D scanner was used to scan the Commercial off-the-Shelf (COTS) quadcopter shown in Fig. 37. It uses laser scanning technology to scan the object. Using the MakerBot Digitizer scanner, we developed an accurate representation of the quadcopter, as illustrated in Fig. 37b.

The effect of the frame is negligible since it is composed of a low permittivity dielectric. Thus, we removed the frame and retained the same wire distribution as shown in Fig. 37c and Fig. 37d, which

show two different views of the UAV wiring system. In Fig. 37c and Fig. 37d, the wires' lengths and diameters match the values in the actual scanned UAV, and all the IC components are represented by blue ports to which an arbitrary impedance can be assigned. Twenty-four loads were connected to the wiring system to act as a rough representation of the various UAV devices. Four loads are added at the center of the UAV to represent the input impedance between the pins and the rectangular ground plane of the controller. The controller generates at these four pins the signal that controls the speed of the four motors. The rectangular ground plane is assumed to be $85 \text{ mm} \times 48.5 \text{ mm}$. Without loss of generality, we select the load under test (LUT) to be one of the four loads at the controller, as shown in Fig. 37c. However, the LUT can be varied to be any of the twenty-four loads in the system. Additional loads can be added to the wiring system to better approximate the actual UAV devices. However, the system in Fig. 37 represents a compromise between simplicity and accuracy in representing the UAV. The electromagnetic compatibility of the proposed model will be examined using the ECA in the following subsections.

As shown in Fig. 1, the input impedance, Z_{in} , is a vital parameter in calculating the coupling to the LUT. Therefore, the accuracy of the circuit representation of the input impedance is an important factor to be considered. The input impedance can be represented by different circuit topologies. In this work, we studied two circuit topologies for the input impedance representation. The two representations are categorized as (i) *Circuit 1*: In

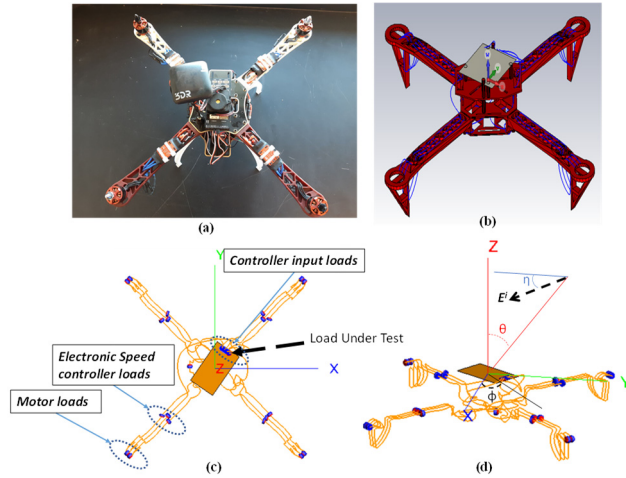


Fig. 37: (a) UAV picture, (b) UAV quadcopter wiring diagram above a dielectric frame, (c) The top view of the proposed model of the UAV wiring system in (a) and (b), (d) side view of the proposed model of the UAV wiring system showing the UAV model orientation with respect to the angles θ , ϕ , and η .

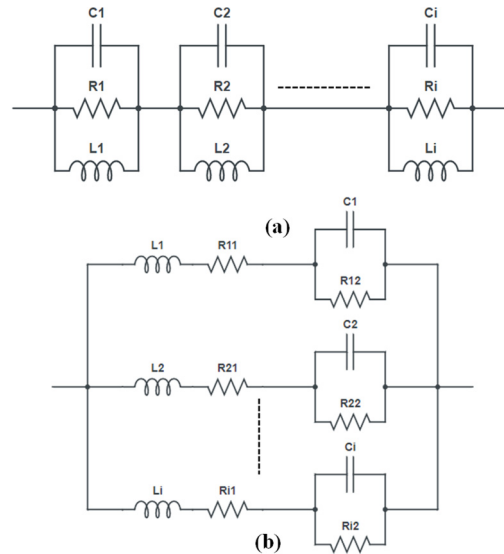


Fig. 38: RLC circuit representation of Z_{in} at the load of interest (a) Circuit 1 (b) Circuit 2.

this circuit representation, each parallel RLC branch of the network shown in Fig. 38a is developed to represent a single resonance of the input impedance of the system [11] (ii) *Circuit 2*: In this circuit representation, the input impedance is modeled as a summation of N arbitrarily weighted poles. Poles typically exist in conjugate pairs. Each pair can be represented by a Second Series-Equivalent-Circuit (SSEC) branch consisting of an inductor, a capacitor, and two resistors connected Fig. 38b [13].

The differences between the two circuit topologies are illustrated as follow:

- (i) *Circuit 1*: the RLC components' values can be calculated from the input impedance of the system by solving the following two equations [11].

$$B.W_i = \frac{1}{2\pi R_i C_i} \quad (3)$$

$$f_{r_i} = \frac{1}{\sqrt{L_i C_i}} \quad (4)$$

where f_{r_i} is the resonance frequency of the i^{th} peak of the input impedance response, $B.W_i$ is the bandwidth of the i^{th} peak of the input impedance response, R_i is the peak value of the input impedance at the i^{th} resonance. By solving (3) and (4), the corresponding RLC values of the entire input impedance response can be calculated. Next, the parallel RLC branches can be connected in series, as illustrated in Fig. 38a, to form the overall input impedance representation of the system.

- (ii) *Circuit 2*: Antonini *et al.* illustrated that the rational function $F(s)$ of any given response could be written as follows [14]:

$$F(s) = \sum_{i=1}^N \frac{r_i}{s + p_i} \quad (4)$$

where N is the number of poles, $s = j\omega$ is the complex frequency, r_i and p_i are the residues and poles, respectively. The parameters r_i and p_i can be estimated using the vector fitting technique detailed in [13]-[14]. The values of R_{i1} , R_{i2} , L_i , and C_i in Fig. 3b can be calculated using the values of r_i and p_i as described in detail in [14]. It is worth mentioning that this method might generate negative impedance values, which can be replaced by an equivalent positive impedance and a parallel current-dependent-current-source (CDCS). That is, *Circuit 2* is, in general, more complex than the *Circuit 1* representation. However, unlike the representation in *Circuit 1*, the value of N can be smaller or larger than the number of Z_{in} peaks in the frequency range of interest. Moreover,

N can be increased progressively to achieve the desired level of agreement between the Z_{in} calculated using the full wave solver and the Z_{in} calculated using the Circuit 2 representation in Fig. 38b.

For the UAV wiring system shown in Fig. 37c, Fig. 39a and Fig. 39b show the magnitude and phase, respectively, of Z_{in} at the port of the LUT. Fig. 39a and Fig. 39b show a comparison between the magnitude and phase of Z_{in} calculated using the Full-wave solver, FEKO [10], and the corresponding values calculated using the two different equivalent circuit representations in Fig. 38. Since there are six peaks in the response shown in Fig. 39a, the Circuit 1 representation will consist of six RLC network branches to represent the full-wave input impedance of the UAV model. For a fair comparison in terms of circuit complexity, we also used 6 branches for the Circuit 2 representation in Fig. 39a and Fig. 39b. Figure 39a illustrates that Circuit 1 agrees better with the full-wave Z_{in} at low frequencies than Circuit 2. For example, at the first resonance 0.15 GHz, the relative differences between the magnitude of the full-wave Z_{in} compared to the Circuit 1 and Circuit 2 representations are 1.4 % and 74.4 %, respectively. Moreover, at the intermediate frequency range, between 0.3 to 0.6 GHz, Circuit 2 missed two consecutive peaks while Circuit 1 response perfectly matched the full-wave Z_{in} . Contrastingly, at the high-frequency range > 0.6 GHz, Circuit 2 provides a better match to the full-wave response.

Since the Circuit 2 representation is based on the fitting technique, the value of N and the number of branches can be increased to improve the Z_{in} representation. Increasing N increases the complexity of the SPICE simulations, but it is still orders of magnitude faster than the full-wave solvers. Figure 39c and 39d show the comparison between the magnitude and phase of Z_{in} calculated using FEKO, and Circuit 2 when using four RLC branches/resonance, i.e., a total of $6 \times 4 = 24$ circuit branches connected as shown in Fig. 38b. The response of the improved circuit representation of Circuit 2 perfectly matches the full-wave Z_{in} . In summary, when the same number of branches are used, Circuit 1 can be better than the Circuit 2 representation up to a certain

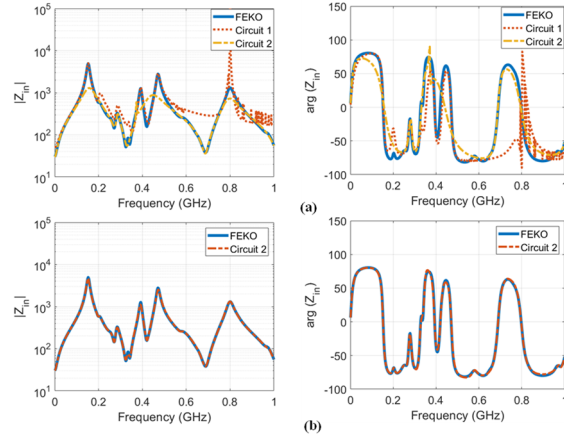


Fig. 39: Comparison between the magnitude and phase of Z_{in} calculated using FEKO, Circuit 1, and Circuit 2 when using: (a) single RLC branch/resonance, (b) 4 RLC branches/resonance.

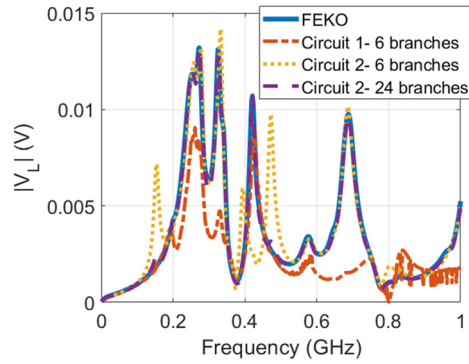


Fig. 40: The induced load voltage across the LUT calculated using different circuit topologies.

maximum frequency value, e.g., 0.6 GHz in Fig. 39. However, the Circuit 2 representation is much better than the Circuit 1 representation in agreeing with Z_{in} , especially when the number of circuit branches is increased.

An accurate representation of Z_{in} is required to ensure better accuracy in calculating the coupled voltage to the LUT. For example, we set all the loads of the UAV wire system to be 10Ω . The UAV is, then, excited by a 1 V/m plane wave excitation. The excitation angle of incidence is chosen to be $\theta = 45^\circ$ and $\varphi = 45^\circ$, and the polarization angle is chosen to be $\eta = 45^\circ$. Figure 40 shows the load voltage at the LUT calculated using the two-circuit representation according to (1). Figure 40 illustrates that V_L calculated using the Circuit 2 representation with 24 branches provides perfect agreement with the full-wave V_L . On the other hand, using Circuit 2 representation with 6 branches provides the worst representation of the full-wave Z_{in} leading to the worst estimation of V_L . Hence, an accurate representation of Z_{in} of the system is essential. However, the ECA evoked in this work indicates that both the input impedance and the open-circuit voltage are important in estimating the electromagnetic compatibility of the UAV. In the next section, the effect of the open-circuit voltage V_{oc} is discussed in detail.

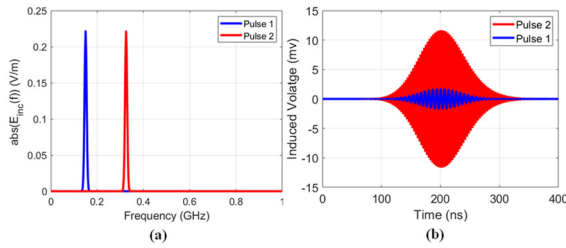


Fig. 41: (a) The frequency domain of the gaussian pulse excitation resonates two different resonance frequencies. (b) the corresponding time domain load voltage due to the gaussian excitation in (a)

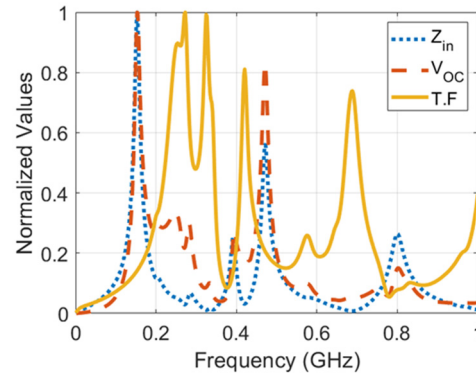


Fig. 42: The normalized values of the open circuit voltage, the input admittance, and the ratio between the two (TF).

This section expands the study to show that the open-circuit voltage plays a significant role in estimating the coupling to the system. To highlight this role, we set all the loads of the UAV wire system to be 10Ω , and we varied the center frequency of the incident pulsed excitations. That is, all the blue dots in Fig. 37 are set to be 10Ω . Figure 41 shows the comparison between the time-domain load voltage for a Gaussian excitation with two different center frequencies 0.15 GHz, the first peak of V_{oc} and Z_{in} , and 0.35 GHz. The two Gaussian pulses have the same peak amplitude, 1 V/m, and the same bandwidth of 10 MHz. The excitation angle of incidence is chosen to be $\theta = 45^\circ$ and $\varphi = 45^\circ$, and the polarization angle is chosen to be $\eta = 45^\circ$. The magnitude of the induced voltage at the load under test is higher when the Gaussian pulse excitation is centered around 0.35 GHz and not 0.15 GHz. That is, the maximum coupling does not occur at the maximum of V_{oc} or

Z_{in} , but it occurs at the maximum of the voltage-divider Transfer Function, $TF = V_{oc}Z_L/(Z_L+Z_{in})$. Figure 42 shows the normalized Z_{in} , V_{oc} , and the TF. Clearly, the maxima of the TF do not necessarily correspond to the maxima of V_{oc} or Z_{in} , indicating the importance of calculating the TF to predict the critical frequencies that maximize the coupled voltage to a LUT.

As illustrated in the previous section, ECA is an efficient approach to predict the frequencies where the coupling to a load of interest will be high/low based on its TF. However, the load values may also significantly impact the ECA components: Z_{in} , V_{oc} , and TF. Therefore, in this section, we will study the effect of different loads on predicting the frequency ranges of high/low coupling to a particular load of interest. Table I summarizes the load variations

TABLE I
LOAD DISTRIBUTION OF THE PROPOSED UAV WIRING SYSTEM

Case	Controller Input Load	All the Other Loads
1	10	10
2	10	2500
3	2500	10
4	2500	2500

in the studied cases. To increase the load variability, the loads were divided into 2 categories: (i) Loads at the input of the controller and (ii) all other loads. In all studied cases, the LUT is fixed to 10Ω , whereas all other loads are changed as described in Table I. Figure 43a shows the input impedance of the system for the four studied cases. Clearly, the input impedance is sensitive to the load selection. For example, comparing the response of Case 1 with Case 2 shows that the resonance frequencies are quite different because in Case 2 the high load impedances act as open circuits, which shorten the electrical length of the system. However, comparing Case 1 and Case 3 shows no variations in the resonance frequencies but rather on the magnitude of the input impedance. Therefore, the loads representing the UAV devices play an important role in the coupling problem.

Similarly, the load selection can affect the V_{oc} across the LUT. To test the effect of the load selection on V_{oc} , the UAV is excited by a 1 V/m plane wave. The excitation angle of incidence is chosen to be $\theta = 45^\circ$ and $\varphi = 45^\circ$, and the polarization angle is chosen to be $\eta = 45^\circ$. Figure 43b shows the V_{oc} of the system for the four studied cases. Clearly, the V_{oc} is also sensitive to the loads. It is worth mentioning that V_{oc} depends on the excitation angle. That is, changing the direction of the incident wave or the polarization will vary V_{oc} . However, Z_{in} is completely independent on the excitation.

Similar to the analysis in the previous section, the TF for all 4 studied cases is calculated. Again, the TF for the 4 studied cases confirms our observation that, for complex wire systems and load distributions, the TF response does not necessarily show the same peaks as the V_{oc} or Z_{in} , and therefore, the TF needs to be explicitly calculated. For example, in Case 1 and Case 3, Z_{in} in Fig. 43a and V_{oc} in Fig. 43b peak at 0.15 GHz, but the TF does not. On the other hand, at 0.7 GHz the

magnitudes of both Z_{in} in Fig. 43a and V_{oc} in Fig. 43b are minimum. However, the TFs of both cases show peaks at this frequency, as shown in Fig. 43c. Similarly, The TF for Case 2 and Case 4 peaks at 0.9 GHz while the magnitudes of both Z_{in} in Fig. 43a and V_{oc} in Fig. 43b are minimum.

An interesting feature of the input impedance response of the 4 Cases is the low magnitudes at the frequency range between 0.2 and 0.4 GHz. For low values of Z_{load} , the TF can be simplified to: $T.F \approx \frac{V_{oc}}{Z_{in}}$. Hence, the TF will peak at the frequencies where Z_{in} is minimum. That is, the frequency range between 0.2 and 0.4 GHz is the most critical frequency range of the system because the TF will always peak at this range. Since Z_{in} is independent of the excitation, this frequency range can be predicted to cause the maximum coupling to the LUT on average when the excitation direction is varied. This prediction was achieved based on the ECA TF with no trial and error, which shows the usefulness of this technique.

To test the ECA TF predictions, the UAV model was excited by a 1 V/m plane wave. Moreover, 325 different angles of incidence, θ , and ϕ were tested where θ varies from 0° to 180° in 15° steps and ϕ varies from 0° to 360° in 15° steps. The polarization angle is fixed at 45° . The induced voltage across the load is averaged over all the incident angles and plotted in Fig. 44. Clearly, all the four studied cases show at least one peak

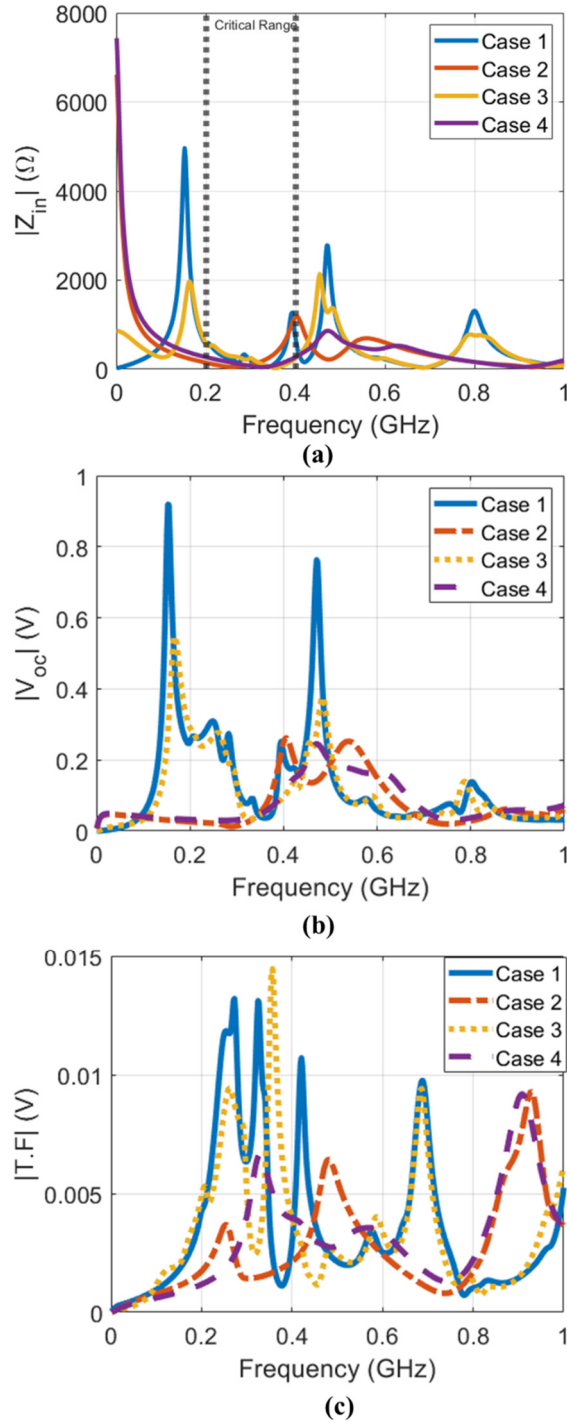


Fig. 43. The input impedance of the system for all 4 studied cases, (b) the magnitude of the open-circuit voltage across the load for all 4 studied cases, (c) the magnitude of the induced voltage across the load (T.F) for all 4 studied cases.

within the critical frequency range predicted by the input impedance of the system shown in Fig. 43a.

The average magnitude of the induced voltage is not the only figure of merit to validate the observations of the ECA. That is, the induced voltage across the load for certain incident angles might dominate the average. Therefore, we tested the probability of the induced voltage exceeding a certain threshold when the direction of the incident wave was varied as previously described. Figure 44b shows the probability of the load voltage exceeding an arbitrary threshold of 5 mV for the four studied cases. The threshold can be tuned to match the value needed to create the desired effect. Each of the four load distribution cases show a maximum probability of exceeding this threshold at a different frequency range. For example, Case 1, shows the highest probability at ~ 0.25 GHz, Case 2 and Case 4 show the highest probability at ~ 0.9 GHz, and the highest probability of Case 3 is at ~ 0.35 GHz. However, all four cases have a significant probability at the critical

frequency range, 0.2 GHz to 0.4 GHz, as predicted by analyzing the Z_{in} of the wires. That is, the wires are acting as a bandpass filter in this frequency range. Hence, regardless of the load impedance, the load voltage has a very high chance to peak at the critical frequency range.

3. Findings and Conclusions

Over the last few years, we developed a wide range of computational tools to quantify and predict RF coupling to a wide range of wires/traces configurations. These computational tools can be classified into 2 main categories: 1- Characteristic Modes Analysis (CMA) and 2- Equivalent Circuit Approach (ECA). The developed computational tools are combined into a single package for the general benefit of ONR and its contractors. The package is titled “**PECNEC: Predictive-package for Electromagnetic Coupling to Nonlinear-electronics using Equivalent-circuits & Characteristic-modes**”. The objective of PECNEC is to predict the waveform envelop that will cause electronic upset, by maximizing the coupled voltage and power, to permutations of

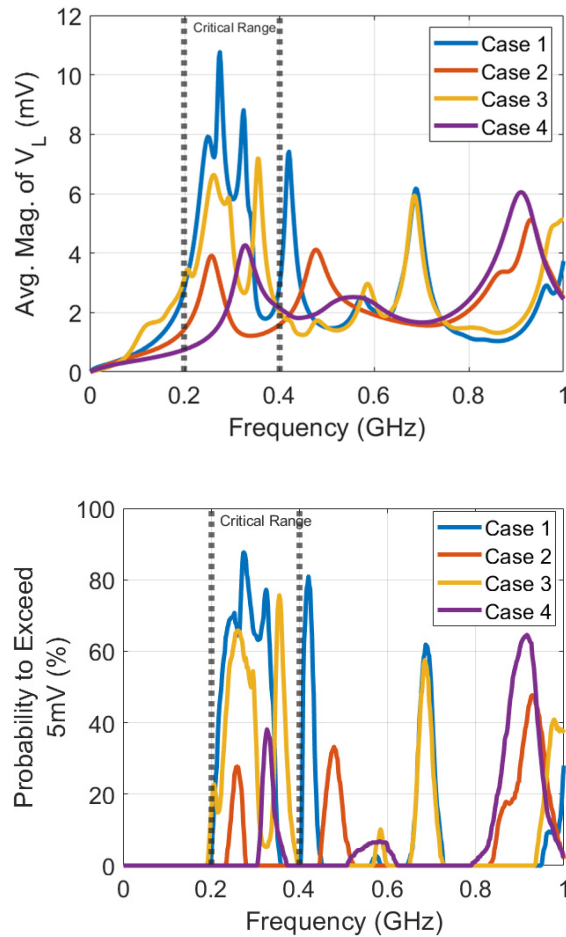


Fig. 44: (a) The average magnitude of the induced voltage over all angles of incidence, (b) The probability of the load voltage, for the four studied cases, to exceed 5 mV.

U // Distribution A

linear/non-linear loads in any wire topology/geometry. To the best of our knowledge, such a package does not exist and there is a strong need for accurate effects-prediction tools, with a low computational burden, to feed into JREM-like software.

The proposed PECNEC is a hybrid package that combines ECA with CMA to determine the RF-induced overvoltage conditions on linear/non-linear circuit elements using SPICE solvers. ECA is $\sim 100x$ faster than full-wave simulations with no loss in accuracy. ECA can also predict the optimum waveform to effect, or the overvoltage conditions on a circuit due to a given waveform. On the other hand, CMA can predict the optimum incident angles (θ , ϕ) and polarization (η) for the excitation. The first version of the package will handle a maximum of two nonlinear/linear loads to demonstrate the art-of-the-possible.

Briefly, PECNEC involves three main modules: the Input Module, the Processing Module, and the Output Module, as shown in Fig. 45. The Input Module involves defining the wire geometry, the load characteristics, and the excitation pulse properties. The package will handle arbitrary-shaped wire loops. Thus, wires can be of different types (regular, twisted pair, etc), different sizes (millimeter to meter range), and different shapes (straight, curved, random). The Processing Module involves performing two full-wave simulations for the ECA. After that, much faster circuits simulations can be used to simulate RF coupling to the user-defined nonlinear loads that will be connected to the wiring system. CMA as part of the processing module allows us to predict optimum incident angles (θ , ϕ) and polarization (η) to maximize the coupling to the load. In the Output Module, PECNEC can calculate the coupling quantities (voltage, current, power, energy, etc.) if the user provides a specific excitation. If the user specifies a threshold and/or the “Absolute Maximum Ratings” specified in the loads’ datasheet, PECNEC will predict the following characteristics for the incident pulsed excitation: Optimum center frequency, Optimum angles of incidence/polarization, and a tradeoff between the excitation amplitude and excitation PRF to achieve the desired threshold. The optimization process is computationally efficient since it will require a maximum of 2 full-wave simulations and use instead several highly accelerated equivalent circuits simulations in SPICE.

The user will also be able to add a “Tolerance Level” that will be used to perturb the load characteristics. This will prevent the user from getting false conclusions that will only be valid for a specific unrepeatable configuration.

In terms of the software that the user must have in order to execute the first version of PECNEC, the user is required to have a MATLAB license, A FEKO license, and LTspice (Open Source). The PECNEC package is currently being updated to allow for different solvers and to support more complex wiring configurations.

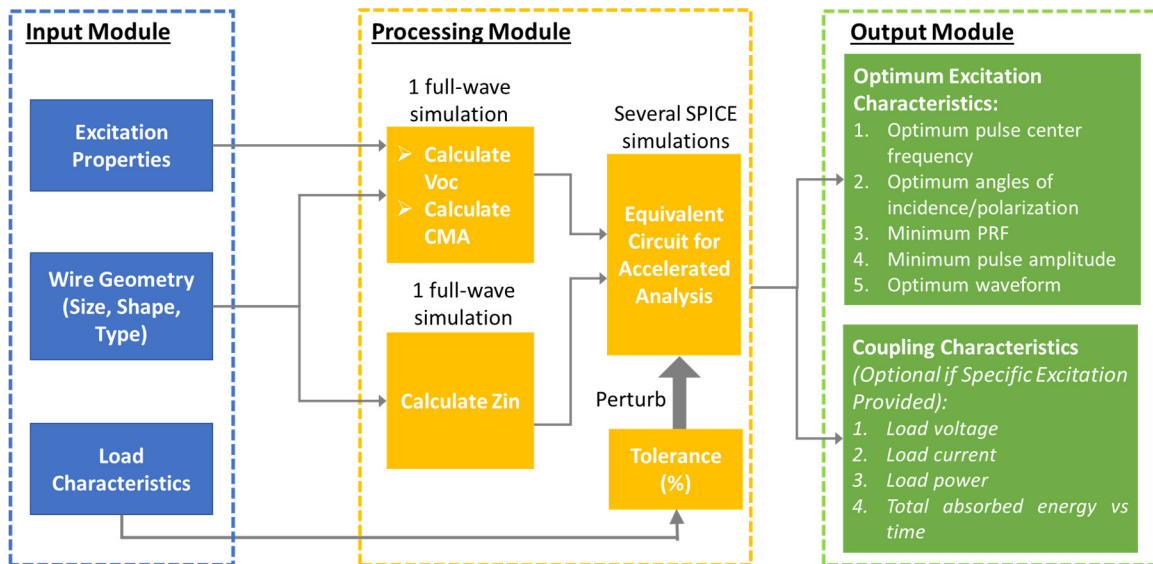


Fig. 45: Flowchart of PECNEC

4. Plans and Upcoming Events

The following improvements are currently planned for PECNEC:

1. Expand the number of solver options based on users' feedback.
 - a. Full-wave solver options: FEKO, CST MWS, COMSOL, and an in-house MOM solver for Arbitrary Thin Wires (ATW)
 - b. Circuit solver options: LTspice, Multisim, etc.
2. Study different equivalent circuits for the ECA to improve the accuracy of the Z_{in} representation.
3. Expand the number of wires and loads
4. Add the effect of the environment e.g. ground planes, enclosures, etc.
5. Build an electronics library compatible with PECNEC by developing black-box equivalent circuits for common electronics. The S-parameters of each component will be measured, translated to impedance/admittance, converted to an equivalent circuit using the black-box macromodeling and the vector-fitting technique [15].

5. Transitions and Impacts

The platform developed in this work, PECNEC, will be augmented with adequate Graphical User Interfaces (GUI) and documentations and presented for the general use of ONR and its defense contractors, e.g. Verus Research (<http://www.verusresearch.net/>). Moreover, the results generated in this work were used as preliminary results for a DARPA WARDEN grant.

References:

- [1] M. Cabedo-Fabres, E. Antonino-Daviu, A. Valero-Nogueira and M. F. Bataller, "The Theory of Characteristic Modes Revisited: A Contribution to the Design of Antennas for Modern Applications," *IEEE Antennas and Propagation Magazine*, vol. 49, no. 5, pp. 52-68, Oct. 2007, doi: 10.1109/MAP.2007.4395295.
- [2] A. Kalantarnia, A. Keshtkar, and A. Ghorbani, "Predicting the effects of HPEM radiation on a transmission line terminated with linear/nonlinear load in perforated metallic enclosure using fddm/vf," *IEEE Trans. Plasma Sci.*, vol. 48, no. 3, pp. 669–675, Mar. 2020, doi: 10.1109/TPS.2020.2968759.
- [3] R. Michels, M. Kreitlow, A. Bausen, C. Dietrich, and F. Gronwald, "Modeling and verification of a parasitic nonlinear energy storage effect due to high-power electromagnetic excitation," *IEEE Trans. Electromagn. Compat.*, vol. 62, no. 6, pp. 2468–2475, Dec. 2020, doi: 10.1109/TEMC.2020.2980976.
- [4] M. Kotzev, X. Bi, M. Kreitlow, and F. Gronwald, "Equivalent circuit simulation of hpem-induced transient responses at nonlinear loads," *Adv. Radio Sci.*, vol. 15, pp. 175–180, Sep. 2017, doi: 10.5194/ars-15-175-2017.
- [5] D. Palur Palanivelu, R. Michels, M. Kreitlow, and F. Gronwald, "The response of nonlinearly loaded antennas to repetitive HPEM excitations as obtained from equivalent circuit models," *Adv. Radio Sci.*, vol. 16, pp. 135–140, Sep. 2018, doi: 10.5194/ars-16-135-2018.
- [6] A. M. Hassan, F. Vargas-Lara, J. Douglas, and E. Garboczi, "Electromagnetic Scattering From Multiple Single-Walled Carbon Nanotubes Having Tumbleweed Configurations," *IEEE Trans. on Antennas and Propagation*, vol. 65, no. 6, pp. 3192-3202, 2017.
- [7] N. Toscani, G. Spadacini, F. Grassi, and S. A. Pignari, "Lumped and Distributed-Parameter Circuit Models of the Electromagnetic Clamp," *IEEE Trans. Electromagn. Compat.*, vol. 58, no. 4, pp. 1007–1015, Aug. 2016.
- [8] L. Badini, G. Spadacini, F. Grassi, S. A. Pignari, and P. Pelissou, "A Rationale for Statistical Correlation of Conducted and Radiated Susceptibility Testing in Aerospace EMC," *IEEE Trans. Electromagn. Compat.*, vol. 59, no. 5, pp. 1576–1585, Oct. 2017.
- [9] F. Grassi, H. Abdollahi, G. Spadacini, S. A. Pignari, and P. Pelissou, "Radiated Immunity Test Involving Crosstalk and Enforcing Equivalence With Field-to-Wire Coupling," *IEEE Trans. Electromagn. Compat.*, vol. 58, no. 1, pp. 66–74, Feb. 2016.
- [10] <https://www.altair.com/feko/>
- [11] R. Michels, M. Willenbockel and F. Gronwald, "A Parametric Study of an Energy Storage Effect due to Nonlinear Components and HPEM-Excitation," *2019 International Symposium on Electromagnetic Compatibility-EMC EUROPE*, 2019, pp. 59-64, doi: 10.1109/EMCEurope.2019.8871855.
- [12] M. Sadraey, "Unmanned Aircraft Design: A Review of Fundamentals," *Synthesis Lectures on Mechanical Engineering*, vol. 1, no. 2, pp. i–193, Sep. 2017, doi: 10.2200/S00789ED1V01Y201707MEC004.
- [13] B. Gustavsen and A. Semlyen, "Rational approximation of frequency domain responses by vector fitting," *IEEE Trans. Power Delivery*, vol. 14, no. 3, pp. 1052-1061, July 1999.
- [14] G. Antonini, "SPICE equivalent circuits of frequency-domain responses," in *IEEE Transactions on Electromagnetic Compatibility*, vol. 45, no. 3, pp. 502-512, Aug. 2003, doi: 10.1109/TEMC.2003.815528.

U // Distribution A

- [15] S. Grivet-Talocia and B. Gustavsen, *Passive Macromodeling Theory and Applications*, Hoboken, NJ, USA: Wiley, 2016.

6. Collaborations

- Professor Daryl Beetner, Missouri University of Science and Technology, Electromagnetic Compatibility Lab
- Associate Professor, Victor Khilkevich, Missouri University of Science and Technology, Electromagnetic Compatibility Lab

7. Personnel

Principal investigator

Anthony N. Caruso, National Academy Member (Y/N)

Co-investigator or Co-PI

Ahmed Hassan, National Academy Member (Y/N)

Business Contact

Linda Daugherty, Leta Moler

Team Members:

Deb Chatterjee, Praveen Rao, John Lancaster, Mohamed Hamdalla, Kalyan Durbhakula, Waleed Al-Shaikhli, Khulud Alsultan, Khadimul Islam, Clayton Kettlewell, Caylin Hartshorn, Benjamin Bissen, Mustafa Yildirim, National Academy Member (Y/N)

8. Students

Undergraduate Students: Clayton Kettlewell, Mustafa Yildirim.

Graduate Students: Benjamin Bissen, John Lancaster, Mohamed Hamdalla, Kalyan Durbhakula, Waleed Al-Shaikhli, Khulud Alsultan, Khadimul Islam

9. Technology Transfer

None

10. Products, Publications, Patents, License Agreements, etc.

Publications resulting from this project:

Archival Publications (publication reference information (article title, authors, journal, date, volume, issue) can be automatically entered using a DOI)

Journal Papers

U // Distribution A

1. K. Alsultan, M. Z. M. Hamdalla, S. Dey, P. Rao, and Ahmed M. Hassan, "Scalable and Fast Characteristic Mode Analysis Using GPUs," *Applied Computational Electromagnetics Society Journal (ACES)*, (In Press), 2022.
2. B. K. Lau, M. Capek, and Ahmed M. Hassan, "Characteristic Modes—Progress, Overview, and Future Perspectives," *IEEE Antennas and Propagation Magazine (In Press)*, 2022.
3. M. Z. M. Hamdalla et al., "Characteristic Mode Analysis Prediction and Guidance of Electromagnetic Coupling Measurements to a UAV Model," *IEEE Access*, vol. 10, pp. 914-925, 2022, doi: 10.1109/ACCESS.2021.3138296.
4. M. Hamdalla, A. N. Caruso, and Ahmed M. Hassan, "Predicting Electromagnetic Interference to a Terminated Wire Using Characteristic Mode Analysis," *Applied Computational Electromagnetics Society Journal (ACES)*, Vol. 35, No. 11, pp. 1318-1319, Nov. 2020, doi: 10.47037/2020.ACES.J.351128.

Journal Papers Under Review/Preparation

1. M. Z. M. Hamdalla, A. N. Caruso, and A. M. Hassan, "Electromagnetic Compatibility Analysis of Quadcopter UAVs Using the Equivalent Circuit Approach," *IEEE Open Journal of Antennas and Propagation*, (Under Review), 2022.
2. M. Hamdalla, W. Al-Shaikhli, J. Lancaster, J. Hunter, L. Yuanzhuo, V. Khilkevich, D. Beetner, A. N. Caruso, and A. M. Hassan, "Field to Wire Coupling: A Characteristic Mode Analysis Approach," *IEEE Transactions on Electromagnetic Compatibility*, (Under Preparation), 2022.
3. M. Z. M. Hamdalla, A. N. Caruso, and A. M. Hassan, "Characteristic Mode Analysis of the UAV Frame Material Effect on its Electromagnetic Compatibility Response," *Progress In Electromagnetic Research*, (Under Preparation), 2022.

Invention Disclosures:

1. D. Beetner, V. Khilkevich, A. Hassan, S. Xia, J. Hunter, A. Harmon, "Rapid Prediction of Electromagnetic Coupling to Electronic Circuits and Harnesses," *Invention Disclosure (Under Preparation)*, 2022.

Conference Papers

1. S. Xia, J. Hunter, A. Harmon, M. Z. M. Hamdalla, A. M. Hassan, C. Hwang, V. Khilkevich, D. G. Beetner, "A Fast Cascading Method for Predicting the Coupling from External Plane Waves to PCBs," *Submitted to the 2022 IEEE International Symposium on EMC+SIPI*, Spokane, Washington, August 1-5, 2022.
2. J. Hunter, S. Xia, A. Harmon, M. Z. M. Hamdalla, A. M. Hassan, V. Khilkevich, D. G. Beetner, "A Segmentation Strategy for Structures with Common Mode Coupling," *Submitted to the 2022 IEEE International Symposium on EMC+SIPI*, Spokane, Washington, August 1-5, 2022.
3. B. Bissen, T. Ory, M. Z. M. Hamdalla, A. M. Hassan, A. N. Caruso, "An Automated Experiment for Parametric Investigation of Voltage Stacking Behavior," *IEEE International Symposium on Antennas and Propagation and USNC-URSI Radio Science Meeting*, Singapore, December 4-10, 2021.

4. M. Z. M. Hamdalla, A. N. Caruso, A. M. Hassan "Predicting RF Coupling to a UAV Wiring System Using the Equivalent Circuit Approach," *IEEE International Symposium on Antennas and Propagation and USNC-URSI Radio Science Meeting*, Singapore, December 4-10, 2021.
5. K. Alsultan, A. M. Hassan, and P. Rao, "Scalable Acceleration of Characteristic Mode Analysis Using Big Data Techniques," *IEEE International Symposium on Antennas and Propagation and USNC-URSI Radio Science Meeting*, Singapore, December 4-10, 2021.
6. M. Z. M. Hamdalla, A. N. Caruso, A. M. Hassan, "A Predictive-Package for Electromagnetic Coupling to Nonlinear-Electronics using Equivalent-Circuits and Characteristic-Modes (PECNEC)," *Directed Energy Systems Symposium*, Washington DC, USA, 25 - 29 October 2021.
7. M. Z. M. Hamdalla, A. N. Caruso, A. M. Hassan, "The Shielding Effectiveness of UAV Frames to External RF Interference," *Directed Energy Systems Symposium*, Washington DC, USA, 25 - 29 October 2021.
8. J. Hunter, S. Xia, A. Harmon, A. M. Hassan, V. Khilkevich, D. Beetner, "Modeling and Statistical Characterization of Electromagnetic Coupling to Electronic Devices," *URSI National Radio Science Meeting*, Boulder, CO, January 4-9, 2021.
9. K. Alsultan, P. Rao, A. N. Caruso, A. M. Hassan, "Scalable Characteristic Mode Analysis: Requirements and Challenges (White Paper)," *Large Scale Networking (LSN) Workshop on Huge Data: A Computing, Networking and Distributed Systems Perspective Sponsored by NSF*, Chicago, IL, 2020.
10. M. Hamdalla, B. Bissen, A. N. Caruso, and A. M. Hassan, "Experimental Validations of Characteristic Mode Analysis Predictions Using GTEM Measurements," *IEEE International Symposium on Antennas and Propagation and USNC-URSI Radio Science Meeting at Montréal, Québec, Canada, July 5-10, 2020*.
11. M. Hamdalla, A. N. Caruso, and A. M. Hassan, "Predicting Electromagnetic Interference to a Terminated Wire Using Characteristic Mode Analysis," *Proceedings of the Annual Review of Progress in Applied Computational Electromagnetics (ACES)*, Monterey, CA, March 22-26, 2020.
12. M. Hamdalla, A. N. Caruso, Ahmed M. Hassan, "Characteristic Mode Analysis of the Effect of the UAV Frame Material on Coupling and Interference," *IEEE International Symposium on Antennas and Propagation and USNC-URSI Radio Science Meeting at Atlanta (2 pages)*, Georgia, USA, 7-12 July 2019.
13. M. Hamdalla, J. Hunter, Y. Liu, V. Khilkevich, D. Beetner, A. Caruso, Ahmed M. Hassan, "Electromagnetic Interference of Unmanned Aerial Vehicles: A Characteristic Mode Analysis Approach," *IEEE International Symposium on Antennas and Propagation and USNC-URSI Radio Science Meeting at Atlanta (2 pages)*, Georgia, USA, 7-12 July 2019.
14. K. Durbhakula, J. Lancaster, J. Hunter, Y. Liu, D. Beetner, V. Khilkevich, D. Chatterjee, A. Caruso, Ahmed M. Hassan, "Electromagnetic Coupling Analysis of Printed Circuit Board Traces using Characteristic Mode Analysis," *IEEE International Symposium on Antennas and Propagation and USNC-URSI Radio Science Meeting at Atlanta (2 pages)*, Georgia, USA, 7-12 July 2019.
15. K. Alsultan, P. Rao, A. N. Caruso, and Ahmed M. Hassan, "Scalable characteristic mode analysis using big data techniques," *International Symposium on Electromagnetic Theory (EMTS 2019)*, San Diego, CA, USA, May 27-31, 2019.
16. M. Z. M. Hamdalla, W. Al-Shaikhli, J. Lancaster, J. D. Hunter, L. Yuanzhuo, V. Khilkevich, D. G. Beetner, A. N. Caruso, and Ahmed M. Hassan, "Characteristic Mode Analysis of

- Electromagnetic Coupling to Wires with Realistic Shapes,” *International Symposium on Electromagnetic Theory (EMTS 2019)*, San Diego, CA, USA, May 27-31, 2019.
17. C. Hartshorn, K. Durbhakula, D. Welty, D. Chatterjee, J. Lancaster, Ahmed M. Hassan, A. N. Caruso, “Crosstalk and Coupling to Printed Circuit Board Metallic Traces with Arbitrary Shapes,” *Proceedings of the AMEREM 2018 Conference*, Aug 27-31, Santa Barbra, CA, 2018.
 18. M. Hamdalla, J. Roacho-Valles, J. Hunter, D. Beetner, Ahmed M. Hassan, A. N. Caruso, “Electromagnetic Analysis of Unmanned Aerial Vehicles Using Characteristic Mode Analysis,” *Proceedings of the AMEREM 2018 Conference*, Aug 27-31, Santa Barbra, CA, 2018.
 19. C. Hartshorn, M. Hamdalla, J. Lancaster, Ahmed M. Hassan, A. N. Caruso, “Electromagnetic Vulnerability of Wires with Arbitrary Shape,” *Proceedings of the AMEREM 2018 Conference*, Aug 27-31, Santa Barbra, CA, 2018.
 20. M. Hamdalla, Ahmed M. Hassan, A. N. Caruso “Characteristic Mode Analysis of Unmanned Aerial Vehicles with Realistic Shapes and Material Composition,” *IEEE International Symposium on Antennas and Propagation and USNC-URSI Radio Science Meeting at Boston*, MA, 2018.

11. Point of Contact in Navy

- Ryan Hoffman, ONR, ryan.hoffman@navy.mil, Date of Last Research Progress Meeting: 05/17/2021
- Matthew McQuage, Naval Surface Warfare Center Dahlgren, matthew.mcquage@navy.mil, Date of Last Research Progress Meeting: 05/17/2021

12. Acknowledgement/Disclaimer

This work was sponsored by the Office of Naval Research (ONR), under grant number N00014-17-1-2932. The views and conclusions contained herein are those of the authors only and should not be interpreted as representing those of ONR, the U.S. Navy or the U.S. Government.

Section II: Project Metrics

Grant or Contract Number: N00014-17-1-2932

Date Prepared: 01/27/2022

Project Title: RF-Coupling Re-visited

Annual Summary Report: [FY21]

PI: Anthony N. Caruso, 816-235-2505, carusoan@umkc.edu

Department of Physics and Astronomy

University of Missouri, Kansas City, MO.

Ahmed M. Hassan, 816-235-6219, hassanam@umkc.edu

Computer Science Electrical Engineering

University of Missouri, Kansas City, MO.

Metrics

Number of faculty supported under this project during this reporting period: **4**

Number of post-doctoral researchers supported under this project during this period: **1**

Number of graduate students supported under this project during this reporting period: **6**

Number of undergraduate students supported under this project during this period: **3**

Number of scientists / engineers / technicians supported under this project during this reporting period: **N/A**

Number of refereed publications during this reporting period for which at least 1/3 of the work was done under this effort: **4 Journal published, 3 Journals under preparation, 20 conference proceedings**

Number of publications (all) during this reporting period: **4 Journal published, 3 Journals under preparation, 20 conference proceedings**

Number of patents during this reporting period: **N/A**

Number of M.S. students graduated during this reporting period: **N/A**

Number of Ph.D. students graduated during this reporting period: **N/A**

Awards received during this reporting period: **N/A**

Invited talks given: **N/A**

Conferences at which presentations were given (not including invited talks above):

- 1. *IEEE International Symposium on Antennas and Propagation and USNC-URSI Radio Science Meeting at Boston, MA, 2018.***
- 2. *AMEREM 2018 Conference, Aug 27-31, Santa Barbra, CA, 2018.***

3. *International Symposium on Electromagnetic Theory (EMTS 2019), San Diego, CA, USA, May 27-31, 2019.*
4. *IEEE International Symposium on Antennas and Propagation and USNC-URSI Radio Science Meeting at Atlanta, GA, 2019.*
5. *IEEE International Symposium on Antennas and Propagation and USNC-URSI Radio Science Meeting at Montréal, Québec, Canada, July 5-10, 2020.*
6. *The Applied Computational Electromagnetics Society (ACES) Conference, Monterey, CA, March 22-26, 2020.*
7. *The 2021 National Radio Science Meeting (NRSM) Conference, Boulder, CO, USA, January 4-9, 2021.*
8. *IEEE International Symposium on Antennas and Propagation and USNC-URSI Radio Science Meeting at Singapore, December, 2021.*

1. **Financial information**

FY 20xx	Total Budget	Obligated This Period	Obligated Cumulative	Expended This Period	Expended Cumulative	Grant/Contract Period of Performance
6.1 (Basic Research Funding)	\$525,340					9/1/2019 – 8/31/2021
6.2 (Applied Research Funding)	N/A					
Total (if both 6.1 and 6.2 funding was used)						

2. **Administrative notes and other items of interest**

- Ahmed M Hassan Co-PI, 09/01/2020 Early Tenure, and Promotion to Associate Professor at UMKC
- Ahmed M Hassan Co-PI, 02/04/2021, 2021 University of Arkansas College of Engineering Early Career Alumni Award. *Description of the Award: “The College of Engineering Early*

*Career Alumni Award recognizes the exceptional professional and personal achievements of University of Arkansas College of Engineering graduates who are within 15 years from their **first** University of Arkansas graduation date. The Early Career Alumni Award will be presented to individuals who are achieving distinction in their fields of endeavor and show significant promise for professional leadership in state, national and international activities.”*

- Mohamed Hamdalla, Ph.D. student and Graduate Research Assistant, 05/14/2021, UMKC Missouri Institute of Defense and Energy (MIDE) Spring Semester Student Spotlight Award.
- Mohamed Hamdalla defended his PhD Dissertation titled “RF Coupling to Realistic Wire Systems in Complex Environments” in December 2021.
- Khulud Alsultan defended her PhD Dissertation titled “Scalable Acceleration of The Characteristic Mode Analysis Computational Toolbox Using Big Data Techniques” in May 2021.
- Waleed Al-Shaikhli defended his MS Thesis titled “Numerical Analysis Of Helical And Log-Periodic Antennas For Short Pulse Applications” in May 2020.
- Kalyan Durbhakula defended his PhD Dissertation titled “Characteristic Mode Analysis of Crumpled Graphene Flakes and a New Green's Functions Evaluation Method for Layered Media” in August 2019
- John Lancaster, Graduate Research Assistant, joined Lawrence Livermore National Laboratory as an Electrical Engineer in 2020.

Acknowledgments:

This work is supported in full by the Office of Naval Research under grant number N00014 -17-1-2932.

The Missouri Institute of Defense and Energy would like to acknowledge and thank multiple members of their staff for their constant support of all operations:

Leta Moler, Mallory Snyder, Lauren Dorsett, James Verzella, Steve Siegel, Allen Dale, and Jeffrey Newhook.